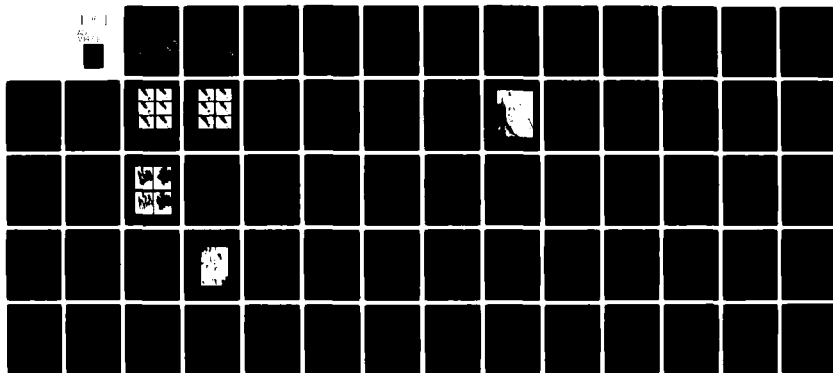
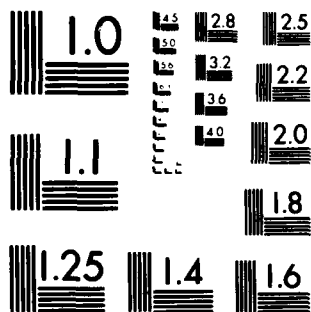


AD-A114 712

VIRGINIA UNIV CHARLOTTESVILLE DEPT OF MATERIALS SCIENCE F/G 11/6
DIRECT STUDIES OF FRACTURE MECHANISMS IN METALS AT HIGHEST MAGN--ETC(U)
MAY 82 H G WILSDORF N00014-75-C-0691
UNCLASSIFIED UVA/525354/M582/102 NL



END
DATE
FILMED
6 82
DTIC



MICROCOPY RESOLUTION TEST CHART
NATIONAL BUREAU OF STANDARDS 1963 A

12

Final Report

Grant No. N00014-75-C-0691

**DIRECT STUDIES OF FRACTURE MECHANISMS
IN METALS AT HIGHEST MAGNIFICATION**

Submitted to:

Office of Naval Research
Department of the Navy
Metallurgy Division - Code 471
800 North Quincy Street
Arlington, VA 22217

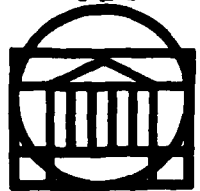
Submitted by:

H. G. F. Wilsdorf
Professor

Report No. UVA/525354/MS82/102

May 1982

**DTIC
SELECTED
MAY 21 1982
H**



**SCHOOL OF ENGINEERING AND
APPLIED SCIENCE**

DEPARTMENT OF MATERIALS SCIENCE

**UNIVERSITY OF VIRGINIA
CHARLOTTESVILLE, VIRGINIA 22901**

82 05 21 038

DTIC FILE COPY

DA114710

DISTRIBUTION STATEMENT A
Approved for public release
Distribution Unlimited

12

Final Report

Grant No. N00014-75-C-0691

DIRECT STUDIES OF FRACTURE MECHANISMS
IN METALS AT HIGHEST MAGNIFICATION

Submitted to:

Office of Naval Research
Department of the Navy
Metallurgy Division - Code 471
800 North Quincy Street
Arlington, VA 22217

Submitted by:

H. G. F. Wilsdorf
Professor

Department of Materials Science
RESEARCH LABORATORIES FOR THE ENGINEERING SCIENCES
SCHOOL OF ENGINEERING AND APPLIED SCIENCE
UNIVERSITY OF VIRGINIA
CHARLOTTESVILLE, VIRGINIA

DTIC
ELECTE
MAY 21 1982
H

Report No. UVA/525354/MS82/102
May 1982

Copy No. 17

DISTRIBUTION STATEMENT A
Approved for public release;
Distribution Unlimited

SECURITY CLASSIFICATION OF THIS PAGE (When Data Entered)

REPORT DOCUMENTATION PAGE		READ INSTRUCTIONS BEFORE COMPLETING FORM
1. REPORT NUMBER	2. GOVT ACCESSION NO. AD-A114710	3. RECIPIENT'S CATALOG NUMBER
4. TITLE (and Subtitle) Direct Studies of Fracture Mechanisms in Metals at Highest Magnification		5. TYPE OF REPORT & PERIOD COVERED Final Report 02/01/69 - 02/28/82
7. AUTHOR(s) H. G. F. Wilsdorf		6. PERFORMING ORG. REPORT NUMBER UVA/525354/MS82/102
9. PERFORMING ORGANIZATION NAME AND ADDRESS University of Virginia School of Engineering and Applied Science Charlottesville, VA 22901		8. CONTRACT OR GRANT NUMBER(s) N00014-75-C-0691
11. CONTROLLING OFFICE NAME AND ADDRESS Office of Naval Research Department of the Navy Arlington, VA 22217		10. PROGRAM ELEMENT, PROJECT, TASK AREA & WORK UNIT NUMBERS
14. MONITORING AGENCY NAME & ADDRESS (if different from Controlling Office)		12. REPORT DATE May 1982
		13. NUMBER OF PAGES
		15. SECURITY CLASS. (of this report) Unclassified
		15a. DECLASSIFICATION/DOWNGRADING SCHEDULE N/A
16. DISTRIBUTION STATEMENT (of this Report) Distribution Unlimited		
17. DISTRIBUTION STATEMENT (of the abstract entered in Block 20, if different from Report) N/A		
18. SUPPLEMENTARY NOTES N/A		
19. KEY WORDS (Continue on reverse side if necessary and identify by block number) crack initiation ductile fracture crack propagation rupture		
20. ABSTRACT (Continue on reverse side if necessary and identify by block number) Techniques for in-situ straining to fracture were developed for use in high voltage and conventional transmission electron microscopes in order to record the dynamical features preceding crack initiation and the subsequent crack propagation in ductile metals. Eight pure metals and alloys have been investigated. It was discovered that dislocation cell walls are the primary sites for microcrack initiation, even in alloys which contain soft second phase particles.		

Unclassified

SECURITY CLASSIFICATION OF THIS PAGE(When Data Entered)

20.

- ✓ Ligament fracture was found to occur by shear which, in low stacking fault metals, was by translation and twinning. The presence of micro-voids and cell wall remnants affected the zig-zag geometry of the crack flank. For macroscopic rupture and for cup-and-cone fracture, the final separation took place by rupture processes in the microstructural regime.

Accession For		<input checked="checked" type="checkbox"/>
NTIS GRA&I		<input type="checkbox"/>
DTIC TAB		<input type="checkbox"/>
Unannounced		<input type="checkbox"/>
Justification		
By _____		
Distribution/		
Availability Codes		
Dist	Avail and/or	
A	Special	



SECURITY CLASSIFICATION OF THIS PAGE(When Data Entered)

SECTION I

INTRODUCTION AND RESEARCH OBJECTIVES

Significant studies of ductile fracture in the microstructural regime were appearing in the literature just two decades ago. Rogers¹ reported on the initiation and distribution of voids in the neck of tensile specimens and Puttick² had observed void initiation at inclusions. Crussard et al.³ had found "dimples" on the fracture surface employing replica techniques for transmission electron microscopy (TEM). It is interesting to note that investigations of ductile fracture concentrated on cup-and-cone fractures but rupture was hardly treated at all. As a consequence, an enormous effort went into studies of (i) void initiation at inclusions and precipitates, and (ii) the subsequent growth of these voids. What was neglected in the course of this development, was the role of workhardening in the fracture process which also has to include the growth and linking of voids for completion of the fracture. Even today this aspect of ductile fracture is not treated by most researchers in this field as a recent paper shows.⁴

The importance of fracture research on metals and alloys containing second phase particles is quite obvious since most technological metals, like steels and aluminum alloys, fall into this category. On the other hand, it is equally important to recognize that the material between inclusions and particles is of reasonable or even high purity and therefore will deform before and after void initiation according to recognized mechanisms of workhardening in pure metals. Although void formation in some alloys can start already after low strains, it should be appreciated that commercial alloys often undergo a reduction in area (RA) of up to 50%. It was one of the major objectives of the project

research to explore the magnitude of workhardening contributions to the various stages of ductile fracture, i.e. its relation to void initiation, void growth, and void coalescence.

To this end, pure metals and alloys have been investigated experimentally. Pure metals subjected to tensile stresses at the appropriate magnitude separate by rupture. From the above discussion it is clear that in precipitation hardened alloys material between voids must suffer extensive plastic deformation during neck formation and the actual rupture process. Depending on the volume fraction of second phase particles the material between voids then represents miniature tensile specimens of larger or smaller size. Picturing these tensile elements as micro test specimens, an investigative technique was developed which permitted the observation of the complete void initiation-growth-coalescence sequence leading to rupture, while the straining was in progress, at magnifications exceeding 100,000x. The technique is now known as high voltage electron microscopy (HVEM) in-situ straining to fracture and enables one to follow the motion of dislocation groups and their specific behavior during plastic deformation to rupture at recording speeds of 30 frames per second. In order to ascertain the validity of our conclusions for ductile fracture mechanisms in general, macroscopic specimens were fractured in an INSTRON tensile testing machine and the fracture surfaces were investigated by scanning electron microscopy (SEM) and by TEM. When analytical electron microscopy became available, these methods were also applied whenever appropriate.

SECTION II

DEVELOPMENT AND APPLICATION OF EXPERIMENTAL TECHNIQUES

Fracture is a dynamic process and consequently much attention has been paid to the propagation of cracks. Regrettably, most data on crack propagation have been inferred from observations which were collected after the fracture process was completed. Direct observations were made only occasionally, namely by high speed optical cinematography. This technique records the spreading of a crack as seen on the surface of a metal with a resolution of a few micrometers. A new technique was developed under this contract using HVEM. Here, crack propagation could be recorded by videotape techniques at 30 frames per second with a resolution of about 1 to 2 nm. The main advantage, however, was the opportunity to see directly the dislocation behavior in front of a moving crack tip.

Compared to conventional TEM, HVEM has the further advantages of higher transmissivity, reduced specimen heating and contamination. With 500 kV electrons one can obtain images with useful resolution from metals whose electron transparent thickness is in the micron range; typical specimen thicknesses are 2 μm for stainless steel and 5 μm for beryllium. Higher acceleration voltages would increase transmissivity somewhat but also brings with it the danger of radiation damage. The threshold voltages for radiation damage are 150 kV for Al, 370 kV for Fe, and 400 kV for Cu, to name only a few. The probability of radiation damage is very low when crack propagation is "fast" during an in-situ experiment, say, 0.5 $\mu\text{m}/\text{sec}$, but slow motion of a crack at 10 nm/sec, and longer times for analytical purposes added to it, may affect the point defect density at the crack tip and thus the mechanism

of crack propagation. Controls were performed with Au which has a threshold voltage of 1.3 MeV for radiation damage, and all experiments yielded results comparable to those obtained earlier from in-situ tests.⁵

Straining stages for the Virginia HVEM were built according to the principles incorporated into an earlier design.⁶ The force to pull a 12 mm long specimen was provided by a spring, the displacement being controlled by a hydraulic system. The purpose of the hydraulic control was to provide a vibration free image on the fluorescent screen at magnification of 100,000x or higher. These stages could be operated at elongation rates between 10 nm/sec and 10^5 nm/sec; the higher speeds duplicated the crack propagation in bulk specimens, and the lower ones were needed for following the crystal defect behavior in front of the crack tip. Care has to be exercised not to strain at the lowest speeds for prolonged periods of time as will be discussed below in Section IV. A detailed description of an HVEM straining stage has been published in 1972.⁷ In-situ fracture processes were recorded by a system utilizing a high performance video tape recorder in conjunction with a low light level TV system (Orthicon). A schematic, Figure 1, shows the arrange-

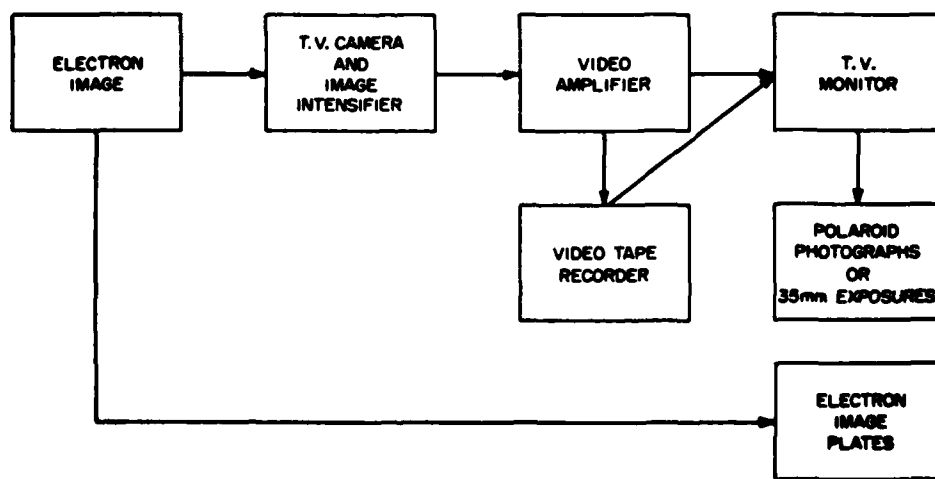


Figure 1. Photographic monitoring system of electron images for the High Voltage Electron Microscope at the University of Virginia.

ment. High image intensification, electronic intensity balancing, frame-by-frame evaluation, and low cost are the main features of a video tape TV system. For measurements of crack propagation, a time scale is provided automatically.

Since it was the objective of this research to study fracture mechanisms in general, macro-specimens were prepared and investigated with conventional techniques such as Instron tensile testing, SEM and others; they are listed in Table I. Specimen preparation and specimens sizes are compiled in Table II; details can be found in the papers referenced in column 5. It should be noted that the X-ray precession method was applied to the study of the severe plastic deformation in the neck of α -Fe crystals by Gardner and Hanscom.⁸ Their results made an important contribution to the understanding of glide processes in the neck

TABLE I
INVESTIGATIVE TECHNIQUES USED IN FRACTURE STUDIES

1. Instron tensile testing (stress-strain data)
2. Bench straining machine (with and without environmental control)
3. X-ray diffraction techniques
4. X-ray precession camera
5. HVEM (in-situ straining)
6. SEM
7. Energy dispersive X-ray analysis
8. TEM (conventional and in-situ straining)
9. TEM (analytical modes)
10. Selected area diffraction (SAD)
11. Microdiffraction

TABLE II
METALS AND ALLOYS INVESTIGATED AND TECHNIQUES OF
INVESTIGATION EMPLOYED

Metal or Alloy	Struct.	Meth. of Investig.						Macroscop. Fracture Method		Type of Spec.	Specimen Size (l = length) (t = thickness at gage length)	Cross Head Speed	Ref.
		In-situ		Post Fract.		Bench Mach.	Instron						
		H	T	T	S								
		V	E	E	M								
		M	(1)	(2)	(3)	(4)	(5)	(6)					
Ag	FCC	X							S	(1) Whiskers l=6-8mm t=0.2-7µm	0.01µm/sec- 1,000µm/sec	10 11	
Al	FCC			X	X	X	X		P	(3) (4) l=20mm; t=0.5mm	10µm/sec	12	
Au	FCC		X	X	X	X	X		P	(2) l=12mm; t=0.2mm (5) l=20mm; t=0.5mm (6) l=50mm; φ=1.5mm	10µm/sec *	5	
Cu	FCC				X	X	X		S	(6) l=50mm; 4x4mm l=120mm; 6x10mm	10µm/sec	12 13	
α-Fe	BCC	X		X	X	X	X		S	(1) Whiskers l=8mm t=10µm (5) " " l=8mm t=0.3mm	0.006µm/sec -800µm/sec	9 16 17 15 18	
Be	HCP	X		X	X	X	X		S	(1) l=12mm; el. pol. perf. (5) l=25mm; t=0.4mm (6) l=25mm; 5=0.4mm	0.1µm/sec-100µm/sec 10µm/sec 1µm/sec-10µm/sec	19 21 20	
304St	FCC	X			X	X			P	(1) l=12mm; el. pol. perf. (6) l=90mm; t=4µm, 6µm, 10µm, 20µm, 43µm, 99µm, 138µm, 1020µm	0.2µm/sec * 1µm/sec	23 24 25	
Al-1.8 w/o Cu	FCC	X		X	X	X	X		P	(1) l=12mm; el. pol. perf. (5) l=40mm; t=0.7mm (6) l=100mm; t=1.7mm	8µm/sec 8µm/sec	26 27 13	

* Across gage length

Type of Specimen: S = single crystal; P = polycrystalline

leading to the final chisel edge.⁹ For detailed information pertaining to the methods and their application to specific fracture studies the reader is referred to the literature references cited in Table II.

SECTION III EXPERIMENTAL RESULTS

Experimental findings will be given first for pure metals and then for alloys. Since fracture mechanisms can be expected to be affected by the mode of plastic deformation preceding the final separation, the pure metals section will be subdivided into FCC, BCC, and HCP structures.

A. Pure Metals

1. FCC Metals

Silver. The first HVEM in-situ experiments were made with Ag. Suitable specimens were obtained by the growth of silver single crystal ribbons through ion reduction.¹⁰ Crystals $1 - 5 \times 10^{-1}$ cm long, $0.1 - 1 \times 10^{-1}$ cm wide and $0.2 - 7 \times 10^{-4}$ cm thick were mounted on a soft copper support which was then attached to the grips of the tensile stage. With deformation of the copper foil the silver crystal was also elongated and continuously observed through an opening in the support foil. The elongation rate of the stage was variable between 1×10^{-6} cm/sec and 1×10^{-1} cm/sec.

The crystal ribbons had a $\langle 110 \rangle$ direction parallel to the tensile axis and their large surface was parallel to an octahedral plane. The reduction of area at fracture was determined by SEM often to exceed 90%. An analysis of the glide geometry has been made and it was found that a predictable rotation around an axis perpendicular to the large surface had always taken place leading to a final stress axis of the crystals in the neck parallel to $\langle 211 \rangle$.¹¹

As shown schematically in Figure 2, fracture started in the necked portion of the crystal beginning from one edge and propagating under

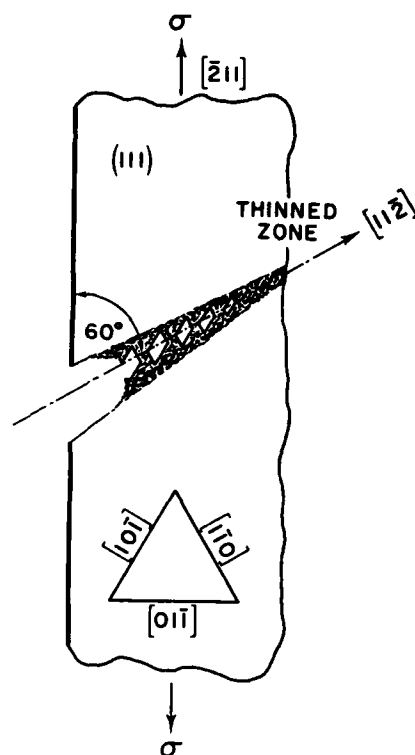


Figure 2. Schematic of Crack Development in the Neck of Ag Crystals.

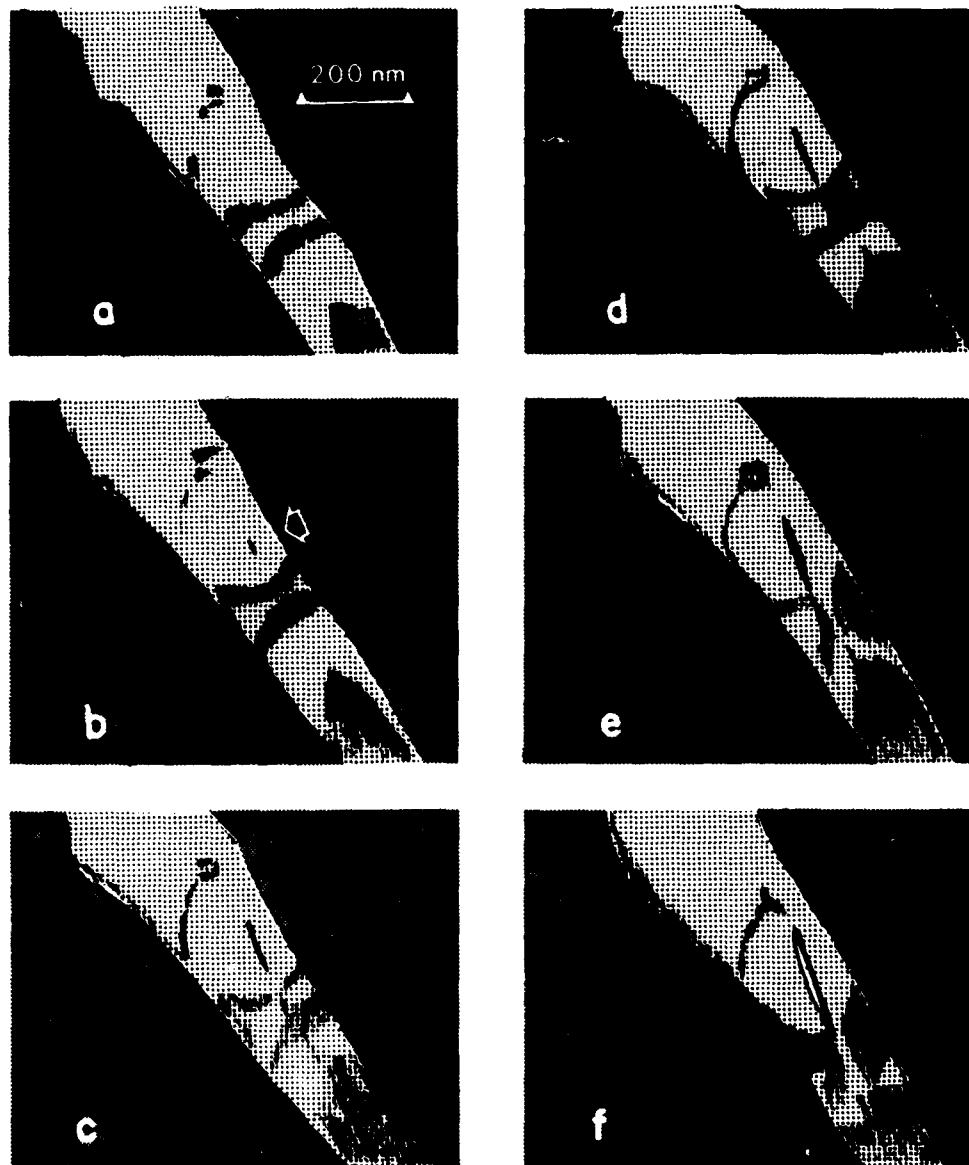
an angle of approximately 60° against the stress axis until failure was completed. The most significant observation, however, was the formation of microcracks in front of the propagating macrocrack. The microcracks were initiated in the most heavily workhardened portion of the crystal which was due to transverse necking visible to about 10^{-3} cm in front of the macrocrack.

The initiation of microcracks took place at distances from each other that were amazingly similar. Consequently, it was predictable where the next microcrack would be formed which aided greatly in the screening of the specific area where the event was going to take place. The regular spacing of nucleation sites for the microcracks in the order of about $0.5 \mu\text{m}$ made it per se highly improbable that they were caused by second phase particles; searching for these, no inclusions were

found in the thinned forward region before fracture nor after the coalescence of the microcracks was completed.

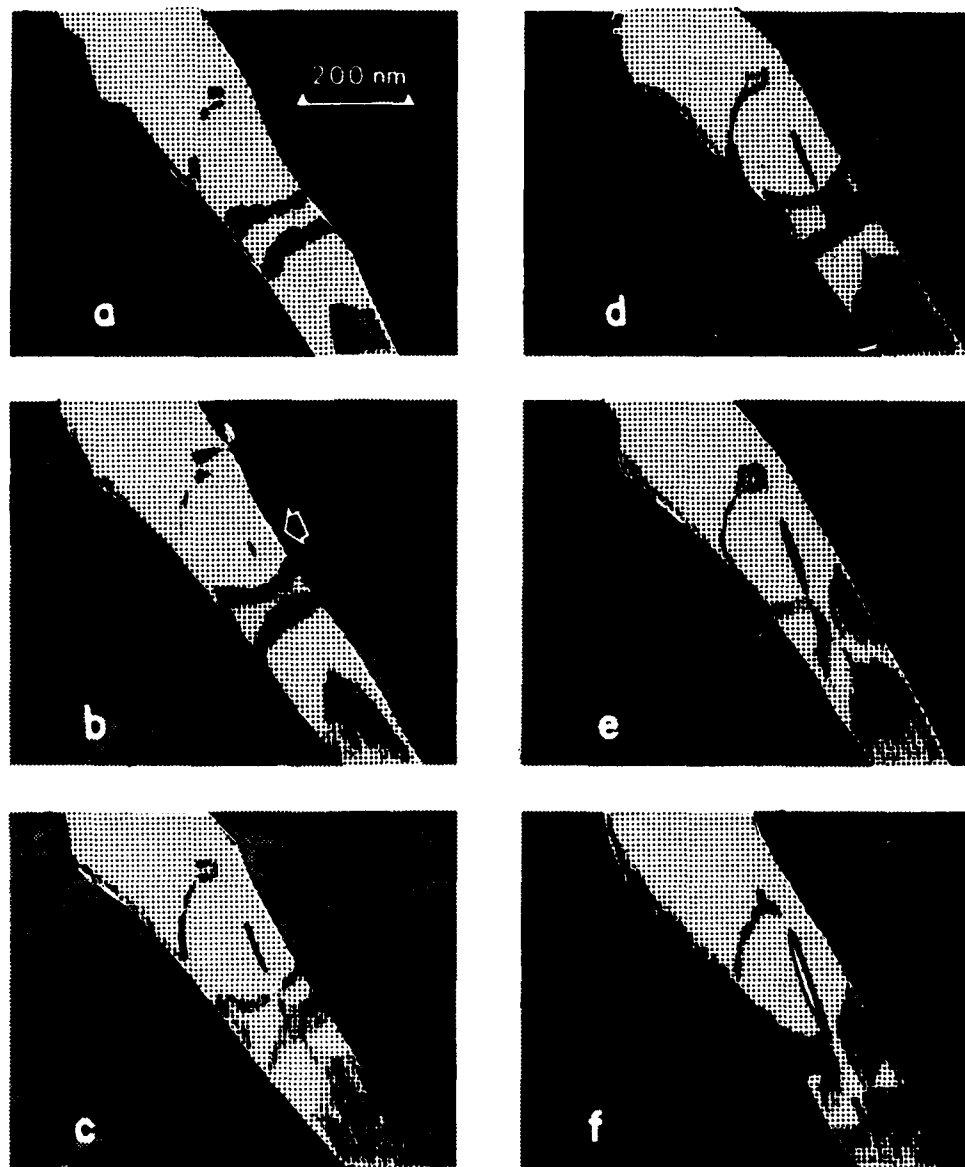
In-situ straining in conjunction with a low light level video tape recording system permitted direct recording of the dynamic processes leading to the development of a sizeable microcrack. The sequence of events can be followed with the help of Figure 3. Due to the difficulty of preparing a representative series of photographs from video frames, graphs published earlier¹¹ are shown. Figure 3a is provided to give an overview of an area ahead of the crack at time 0. Following, one can see in Figure 3b at 4/30 sec that a new narrow contrast area has been formed (arrow) which at 7/30 sec has developed parallel to a $\langle 110 \rangle$ direction (Figure 3c). Further elongations of the contrast zone can be seen at 10/30 sec and 14/30 sec in Figures 3d and 3e. Finally, at 17/30 a slit parallel to the contrast zone has suddenly appeared (Figure 3f). The sequence just described is typical for microcrack initiation at elongation rates of 10^{-5} cm/sec and many similar sequences have been recorded on video tape. The initial length of a microcrack was approximately 200 nm.

The initiation of the microcracks in the transverse neck obviously was taking place under the action of a very complex stress field. This also held true for the growth of holes which were being enlarged strictly by glide on slip systems in accordance with established principles of plastic flow as has been shown by a detailed analysis.¹¹ The geometrical appearance of the holes was enhanced with increasing size until they had the shape of parallelograms with their edges parallel to the two $\langle 110 \rangle$ directions that belonged to the glide systems with the largest Schmid factor. The dislocation density continued to remain extremely



Micrograph	Time	
a	0 sec	plastic zone preceding crack
b	4/30 sec	initial formation of contrast zone (arrow)
c	7/30 sec	contrast zone grows parallel to $\langle 110 \rangle$ direction
d	10/30 sec	elongation of contrast zone through extinction contour almost perpendicular to it
e	14/30 sec	further elongation of contrast zone
f	17/30 sec	opening of slit shaped hole along contrast zone

Figure 3. Schematic Time Sequence Illustrating Microcrack Formation by Micro-cleavage in Front of Propagating Macrocrack in Ag. Drawings are made from individual frames of a video tape recording.



Micrograph	Time	
a	0 sec	plastic zone preceding crack
b	4/30 sec	initial formation of contrast zone (arrow)
c	7/30 sec	contrast zone grows parallel to $\langle 110 \rangle$ direction
d	10/30 sec	elongation of contrast zone through extinction contour almost perpendicular to it
e	14/30 sec	further elongation of contrast zone
f	17/30 sec	opening of slit shaped hole along contrast zone

Figure 3. Schematic Time Sequence Illustrating Microcrack Formation by Micro-cleavage in Front of Propagating Macrocrack in Ag. Drawings are made from individual frames of a video tape recording.

high and it could be concluded that dislocations on active glide systems were leaving the crystal at the edges of the microcrack. Both tensile and compressive stresses were acting, as evidenced by the step geometry of the edges, since the neighboring microcracks must have had a significant influence on the stress distribution. The ligaments between microcracks were becoming thinner continuously but not below a thickness of about 30 nm.

These early experiments showed that cracks in pure Ag did not propagate via the continuous motion of the crack tip as might have been expected from continuum theory. Instead, microcracks were initiated in front of the crack tip, then grew until coalescence occurred. It was not clear at that time, how ten or twelve microcracks could form in front of a macrocrack at fairly regular length intervals.*

Gold.⁵ It was thought advisable to study a non-oxidizing metal. Au of 99.9999 purity was ruptured and investigated by TEM and SEM. In-situ straining to fracture was also carried out with a precision stage in a TEM at 125 kV at elongation rates of 10^{-6} cm/sec and between 10^{-5} and 10^{-4} cm/sec. 1.5 mm thick wire was used for Instron tensile tests and other specimens had dimensions of 3 mm x 12 mm with a thickness between 0.6 and 0.4 mm. All TEM observations were made immediately after or during rupture without additional specimen preparation. Grain size varied between 0.1 and 0.5 μ m.

At higher magnifications the crack flank in ruptured gold crystals is seen in general not as a straight or lightly wavy edge but it consists primarily of serrations which form a triangular zig-zag line. The

* See Appendix I for the chronological order of metals and alloys investigated.

triangular remnants of ligaments are electron transparent and, for the sake of convenience, they will be referred to as ligaments. Their length varies between $0.1\ \mu\text{m}$ and $1\ \mu\text{m}$ and they measure at their base between $1\ \mu\text{m}$ and $2\ \mu\text{m}$. The local direction of stress is approximately perpendicular to their base line. A typical ligament has fairly straight edges, and as indicated by extinction contours is somewhat buckled. Twins are obvious along one edge while the other edge is visibly thinned. Without exception all triangular ligaments were lying in the $\{110\}$ plane. The thinned edge was parallel to $\langle 110 \rangle$ and the other thicker edge parallel to $\langle 112 \rangle$; they included always an angle of 55° or close to it. The relationships between the ligament plane and the glide and twinning geometry is drawn in Figure 4 which shows schematically the (110) plane of the ligament and the four glide planes. Two of them, ACD and BCD, correspond to $(1\bar{1}\bar{1})$ and $(\bar{1}1\bar{1})$ and are perpendicular to (110) . The remaining two, ABC and ABD, corresponding to (111) and $(\bar{1}\bar{1}1)$, are

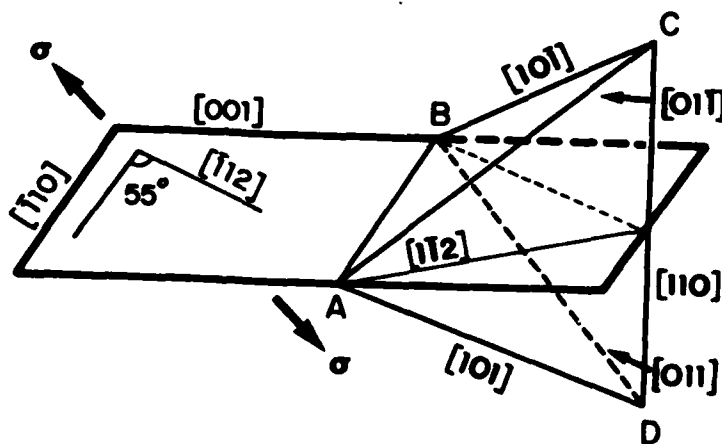


Figure 4. Position of Ligament Plane with Respect to Standard Tetrahedron in FCC Metals.

inclined to the ligament plane at 35° . Since the local tensile axis direction is near $[\bar{1}11]$, the latter two glide planes and $(\bar{1}1\bar{1})$ are of interest for deformation processes. Under these conditions, $[10\bar{1}]$, $[011]$ and $[\bar{1}10]$ can be operative on (111) , $(\bar{1}1\bar{1})$ and $(\bar{1}\bar{1}1)$, but only systems with $[10\bar{1}]$ and $[011]$ could contribute to the thinning of the ligament. Parallel to $(\bar{1}1\bar{1})$ twinning and glide was observed; the possible twinning directions are $[\bar{1}12]$, $[21\bar{1}]$ and $[\bar{1}2\bar{1}]$, and $[\bar{1}01]$ and $[0\bar{1}\bar{1}]$ are the possible glide directions. An understanding of the motion of dislocations on these systems is essential for explaining the final separation.

The thickness variations of ligaments are determined from thickness fringes using the center dark field technique. Typical measurements are shown in Figure 5. The thickness is seen to increase from the edge to its average thickness of 80 nm to 100 nm within a distance of about 50 nm. These measurements permit a decision of whether the

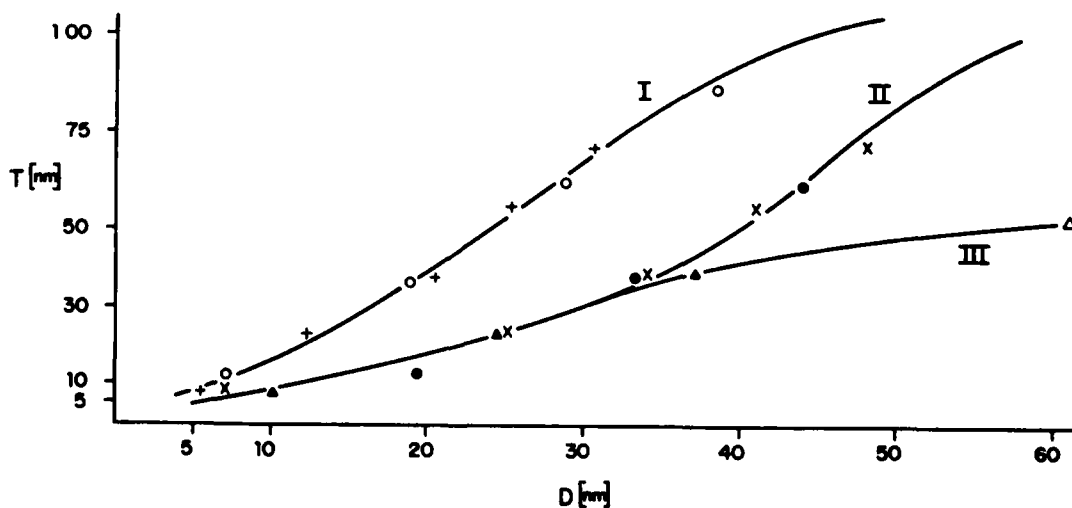


Figure 5. Thickness Profile of Three Ligaments Starting at a $\langle 110 \rangle$ Edge in Au.

crystal sheared off on one glide plane or whether the thinning took place gradually. Since the angle of ligament inclination can be deduced from the data, the latter statement proved to be correct.

Twinning was seen to be a prominent feature when rupture specimens were elongated at a rate of approximately 10^{-4} cm/sec or higher. The final separation took place along $\langle 112 \rangle$, and glide on the two possible systems was also observed. At elongation rates of 10^{-5} cm/sec or slower, glide was predominant and twinning played a minor role only. The triangular ligaments discussed so far did not develop when the elongation rate was reduced to 10^{-6} cm/sec.

Two other microstructural features were discovered in the crack flank: voids and dislocation cell walls. Voids with diameters from 6 nm to 10 nm were made visible by diffraction contrast and in very thin ligament areas holes with comparable diameters were seen. Cell walls were detected through Moiré patterns and by imaging dislocations in the walls. Cell sizes were between 50 nm and 100 nm and misorientations were measured to be from 4° to 13° . Occasionally, distances between cells are not more than 30 nm. Finally, the presence of stacking fault tetrahedra (SFT) should be reported. Their edge length was 4 nm in average.

The observations reported so far were made on specimens which had been designed for microstructural investigations by TEM. Would the same features be produced in cylindrical specimens which presumably would rupture at a chisel point? A 0.15 cm diameter wire was strained in an Instron testing machine to fracture. A neck developed and the wire ruptured at a sharp chisel point as far as a moderate light optical magnification could ascertain. An examination of the ruptured wire by SEM reveals, however, a rugged fracture surface and a multi-



Figure 6. Chisel Point in Au After Rupture. Original Specimen Diameter 0.15 cm.

tude of "points" (see Figure 6). It is obvious that this surface cannot have been created by a uniform shear process but that many local ruptures must have been involved. One end of the ruptured wire was mounted in the TEM and examined. Typical images obtained from one of the many crack flanks of the macroscopic chisel point showed ligaments comparable in size and shape to those discussed above. The zone axis again corresponded to $\langle 110 \rangle$ when the ligaments were viewed with their largest dimension perpendicular to the beam. Dislocation cell walls and twins are clearly visible and stacking fault tetrahedra were seen as well.

Aluminum. 99.9999 purity Al sheet specimens 1 mm thick were ruptured and the crack flanks were studied by SEM and TEM. A macroscopically straight chisel edge was found to have zig-zag shape when viewed at higher magnifications as reported above for Ag and Au. TEM showed dislocation cell walls in most transparent areas, and one instance was recorded where a crack had opened up along a cell wall beginning (or ending) at the junction of two cell walls. Center dark field microscopy revealed that the ligament remnants had vicinal surfaces and became thinner towards their edges. Short dislocations were frequent, which allowed the conclusion that glide had taken place in ligaments in accordance with known selection rules, i.e. that resolved shear stress and low energy configurations of dislocations reached an optimum. Also, voids < 10 nm in diameter were present in most ligament remnants.¹²

Copper. Experiments with 99.999 purity Cu were made with single crystals 4×4 mm and 6×10 mm in cross-section, 60 and 140 mm in length, respectively. Straining the crystals in an Instron tensile testing machine at a cross head speed of about $10 \mu\text{m/sec}$ to rupture,

the chisel edges which had developed in both types of crystals were examined by SEM and TEM.

SEM investigations showed irregular crack flanks and often exposed dimples of various diameters. In TEM studies the similarity of ligaments between Au and Ag was immediately evident. Their orientation was parallel to $\{110\}$, edges were parallel to $\langle 110 \rangle$ and $\langle 112 \rangle$ and many twins were visible along the latter direction. As in Au the ligaments contained many stacking fault tetrahedra. These experiments demonstrated the fact that bulk specimens fracturing by the rupture mode separated by the same mechanisms as in in-situ specimens.¹³ Details will be discussed in Section IV.

2. Bcc Metals

α -Iron. For this study, single crystal iron whiskers were prepared by the hydrogen reduction of ferrous halides. Ranging between 10-500 microns in diameter and about a centimeter in length, the crystals were found to be of various shapes, geometries, and orientations.¹⁴ They were characterized both before and after deformation by observation in the SEM and through the use of the X-ray precession method. The precession method provides information on orientation, indexing of crystal faces, and most importantly, it enables the determination of the deformation character and geometrical history of the crystals.⁸ In addition to their observation in the SEM, the crystals were also studied during deformation under the light microscope. Crystals with their stress axes parallel to $\langle 110 \rangle$, $\langle 111 \rangle$, $\langle 211 \rangle$, or $\langle 100 \rangle$ were strained to fracture in an INSTRON tensile testing machine, as well as in a bench straining device, at elongation rates varying from 7×10^{-6} cm/sec to 8.3×10^{-5} cm/sec. In addition, large ribbons on the order of 4-10 microns thick and 50 microns wide were strained in-situ

in the HVEM. The strengths of these crystals varied systematically with orientation and were found to be in the range of 0.6 to 9×10^8 Pa.

Three-stage hardening was uniformly exhibited by the majority of crystals, as was almost 100% reduction in area, i.e., chisel edge fracture. The chisel edge fracture appeared "crystallographic" in nature. That is, edges of certain orientations were consistently along identical directions, these directions being related to the initial geometry, and reductions in area repeatedly demonstrated the same geometric behavior. The glide geometry of one set of crystals having a stress axis parallel to $\langle 110 \rangle$ will be discussed.

From the deformation geometry it was determined that there had been no distinguishable atomic displacement in any direction other than perpendicular to the $\{110\}$ crystal face. This indicated that the only possible active Burgers vector was normal to the appropriate $\{110\}$ face. With the aid of a cubic (110) standard stereographic projection, it was determined that the only possible active slip systems were $(112)[11\bar{1}]$ and $(11\bar{2})[111]$. Further verification of this fact was obtained through the use of the precession method. Figure 7 indicates this lattice rotation. Increased hardening rates of other samples are due to the additional activation of either the $(12\bar{3})[111]$ and $(123)[11\bar{1}]$ systems simultaneously and/or with further contributions of the $(21\bar{3})[111]$ and $(213)[11\bar{1}]$ slip systems acting together to cause only a slight change in deformation geometry. It could be concluded that the workhardening rates appeared to be directly dependent upon the number of active slip systems. Tables listing the active glide systems for four different tensile axes and the corresponding Schmid factors have been pub-

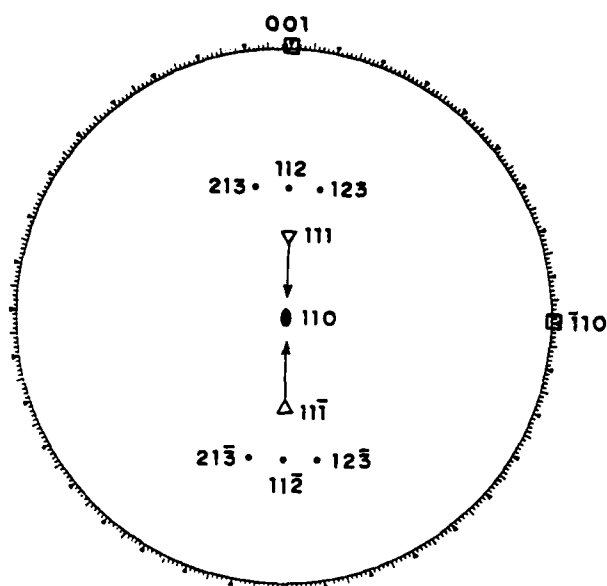


Figure 7. Stereographic Projection Showing Observed Lattice Rotations in α -Fe.

lished.¹⁵ A graphical presentation including the geometry of reduction in area as experimentally observed is provided in Figure 8.

More than 60 crystals were examined during in-situ straining in the HVEM. Selected area diffraction (SAD) spot patterns were made

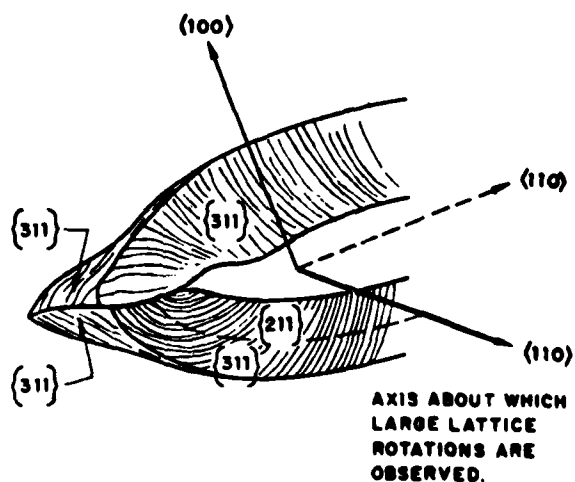


Figure 8. Diagram of a $\langle 110 \rangle$ Oriented α -Fe Whisker Depicting the Crystallography of the Reduction in Area.

from the zig-zag ligament remnants along the fracture flank. They showed average angles of 20° rotation in areas with beam sizes of 500 nm in diameter and the presence of deformation twins. Twinning in the necked area had also been observed with X-ray techniques earlier.¹⁶ Numerous crystallographic relationships between misoriented volume elements have been worked out¹⁷ and a summary was published.¹⁸ Electron micrographs of dislocation cell walls were taken in both, the thinnest as well as the thickest parts of the crack flank and "pin holes" and small thin areas were seen. The analyses of glide processes in the neck, in-situ observations of heavily rotated cells, twinning, and specific contrast changes clearly showed the importance of dislocation cell walls for microcrack initiation for the first time as will be discussed in Section IV.

3. HCP Metals

Beryllium. Preliminary work was carried out by Pollock¹⁹ on rolled polycrystalline Be foil using in-situ HVEM. Since fracture initiated primarily at grain boundaries, however, single crystals were used for this study. The material consisted of six-zone-pass beryllium (Franklin Institute Research Laboratory stock). In order to prevent premature cleavage, slices were cut by acid saw parallel to basal planes which would then under tensile loading deform by prism slip. Specimen size was 12 mm x 2.25 mm x 0.25 mm; for in-situ straining a thin, round area would be prepared by electrolytic polishing in the center of the strip. Fracture was observed on 75 single crystal specimens of which 45 were strained inside the HVEM with the recording techniques illustrated in Figure 1.

Cross head speeds between 10^{-2} cm/sec and 10^{-5} cm/sec were employed by Hedke.²⁰ Since cleavage fracture occurred above 0.025 cm/sec, strain rates below this value were used throughout. The development of dislocation cells was followed by TEM and HVEM in "thick" specimens and in in-situ specimens. Misorientations were measured up to 35° by Pollock²¹; and Hedke²⁰, using Moiré techniques, was able to obtain precision data from the fracture flank in the actual ligaments. The latter measurements showed misorientations between cells from 2° to 17° and cell sizes between $0.1\ \mu\text{m}$ and $0.4\ \mu\text{m}$. Dislocation densities in the cell walls averaged 5×10^{11} dislocations/cm². The stress to bow out dislocation would then have to exceed 5×10^8 Pa.

The cell sizes given above were typical for ligaments and thus give their size in the vicinity of the crack tip. In general they are larger before microcrack initiation occurs. As a consequence of these large cell sizes, it was possible to continue to have considerable electron transparency in the HVEM with increasing strain even in specimens of $2\ \mu\text{m}$ to $5\ \mu\text{m}$ thickness. This in turn made it possible to identify the exact initiation sites where microcracks first appeared. They were seen without exception to be at the dislocation cell walls.²¹ With the continuation of plastic deformation more microcracks appeared at cell walls ahead of the major crack.

In-situ HVEM studies provided also direct experimental evidence as to the growth of the microcrack which always appeared suddenly with lengths between $0.2\ \mu\text{m}$ and $1\ \mu\text{m}$. Microcracks elongated more often than spreading in width. Often the growth followed a cell wall, up to a point, than growing in width. Since the macroscopic crack propagates by the coalescence of microcracks, the path of propagation was seen

again to follow cell walls as documented by Pollock²¹ through in-situ observations. At certain points, for example at branching cell walls, the crack stops and substantial blunting takes place. With increasing overall stress, and naturally affecting the local stress, the material will yield again and the crack continues to propagate. The direct observations of microcrack initiation and propagation made in this study confirmed conclusions which had been based on misorientation measurements of cell walls in $\alpha = \text{Fe}$, and thus started a new approach to the understanding of ductile fracture at the microstructural level.²²

B. Alloys

1. 304 Stainless Steel. In-situ HVEM straining to fracture yielded a number of significant results.²³ Examination of the specimens before straining revealed that the grain boundaries were clean and precipitate free. Grains did not overlap in the beam direction. The initial dislocation density within the grains was very low. The tensile specimens used in this first set of experiments had perforations in the thinned area as a result of the electropolishing technique, and therefore observations will be related to crack propagation. However, these experiments also provided information during crack propagation which indicated the changes in microstructure in front of the crack tip leading to holes opening up a few microns ahead of the crack. Due to the difficulty of producing good half-tone pictures from the TV monitor, Figure 9 has been drawn from single frames.²³ Speed of elongation was $2 \times 10^2 \text{ nm sec}^{-1}$. Cracks move mostly from the electron transparent area into non-transparent material and Figure 9 shows such a crack moving from the right hand side into the field of view. Blunting has taken place and thinning in a broad area has resulted in a semi-trans-

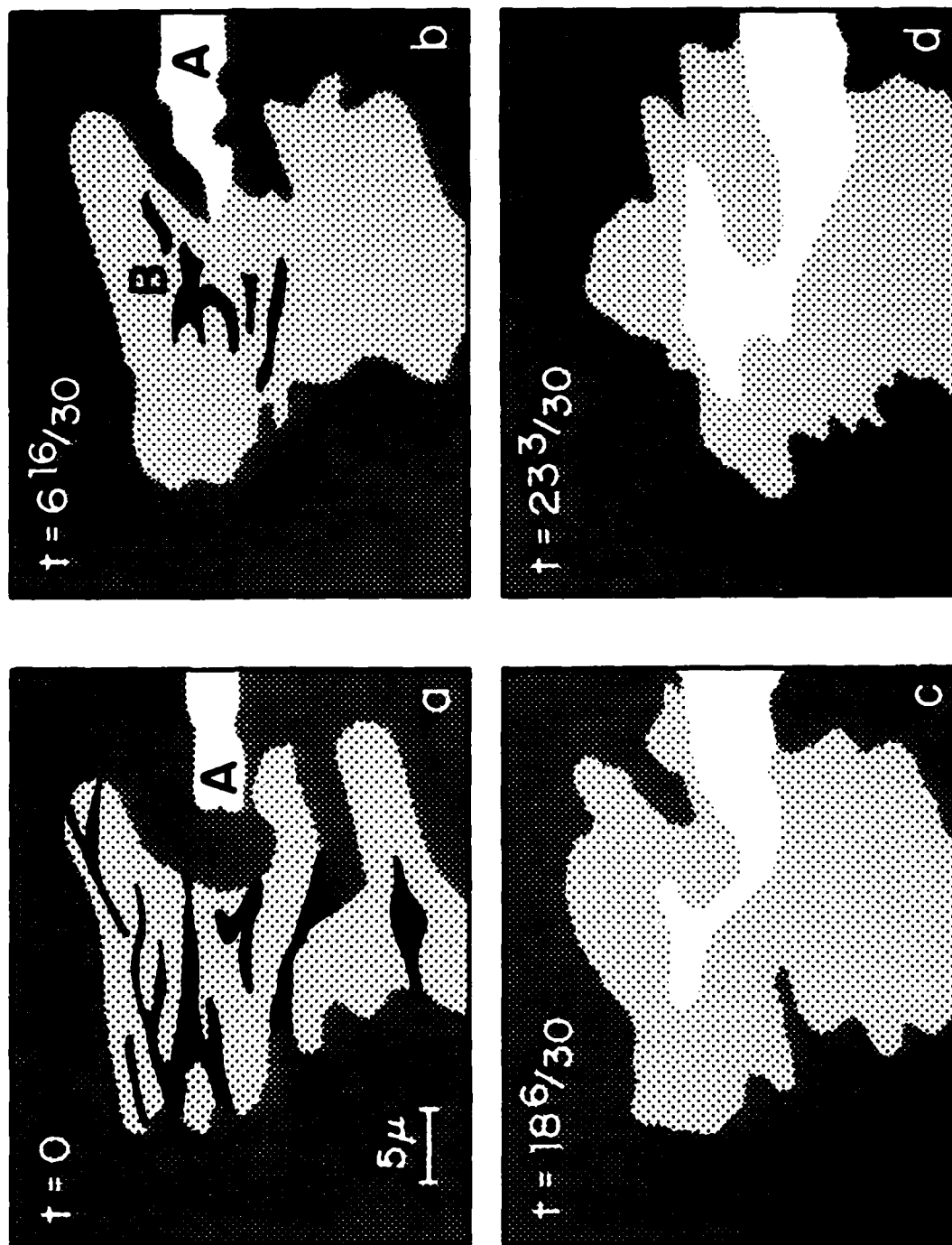


Figure 9. Thinning and Hole Formation Ahead of Blunted Crack Tip in 304 Stainless Steel.

parent region. Clearly, thinning appears to be fairly uniform with dark somewhat fuzzy lines spaced irregularly throughout the area. Spacings between these lines are in the order of a micron. The thickness of the specimen in the semi-transparent area is estimated to be between one and two microns. One can see that in Figure 9b further thinning took place at B and immediately at the crack tip at A. Note the changes in the positions of dark lines. Figure 9c shows the sharpening of the crack tip and the formation of a narrow link to the B area which develops into a hole (Figure 9d). Many sequences of this type were recorded.

In unperforated tensile specimens plastic deformation is observed to originate mainly from grain boundary dislocation sources, and dislocations then move in groups on their slip plane. The dislocations are observed to propagate from one grain to another. With increasing amounts of strain additional slip systems operate and the resultant dislocation structure becomes more complex.

The nature of crack propagation changes quite drastically over the range of thicknesses studied in this investigation, i.e., $\sim 0.1 \mu$ to 3μ . Crack propagation in foils less than 100 nm is characterized by the absence of a plastic zone ahead of the crack tip. No dislocations can be detected in the region immediately adjacent to the crack edge. Crack propagation in this thickness range can be compared in many respects to cleavage. In specimens thicker than about 1μ , crack propagation occurred by the growth and coalescence of holes directly ahead of the crack tip. The interhole distance is about 2μ which is roughly equivalent to the intervoid spacings observed on the fracture surfaces of bulk thickness samples as observed by SEM. Notable is the

plastically deformed zone along the crack; it is about 10 times the foil thickness for this particular thickness regime. Crack flanks are mostly parallel to $\langle 110 \rangle$. In unperforated foils the initiation of holes or micro-cracks can be observed. They occur at the intersection of crossing slip zones by thinning and occasionally holes are seen to initiate at particle-matrix interfaces.

Thin rolled and recrystallized foils in the thickness range between $3.76 \mu\text{m}$ and 1.02 mm were pulled to fracture in an INSTRON tensile testing machine and their fracture surfaces investigated by SEM. The nominal stress-strain curves are shown in Figure 10.²⁴ In the thickness range from $3.76 \mu\text{m}$ to about $50 \mu\text{m}$ the grains are occupying the specimen cross-section and failure is by complete rupture. Dimples of varying sizes are observed at the crest of the fracture surface along

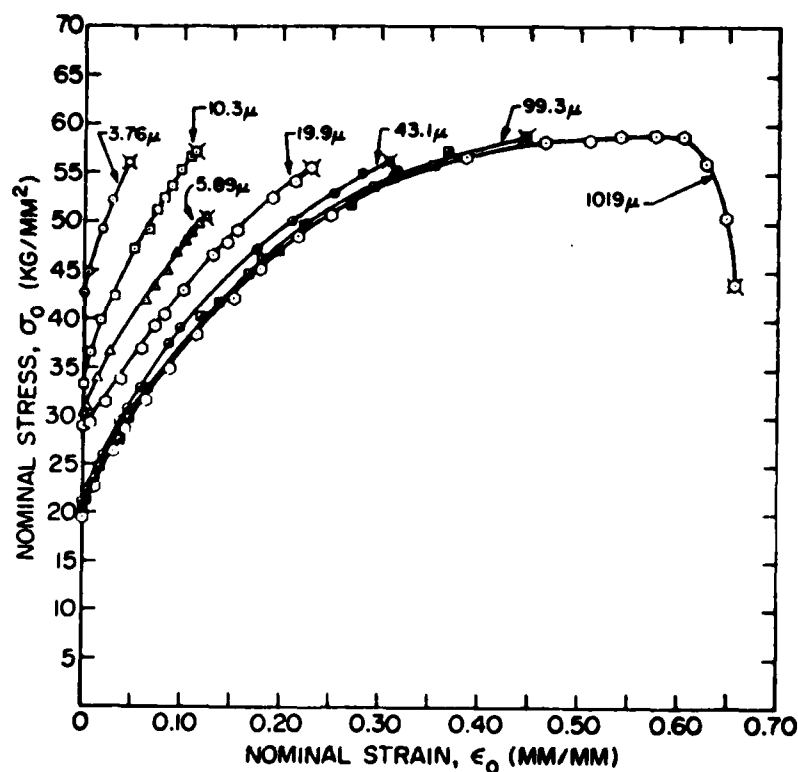


Figure 10. Nominal Stress-Strain Curves of 304 Stainless Steel Foils.

the chisel edge. Thicker foils did not exhibit a RA of 100% but showed wider fracture surfaces which were covered with dimples. Most of the dimples did not relate to the presence of second phase particles as was ascertained by energy dispersive X-ray analysis.²⁵ Measurements on fracture surfaces and the evaluation of mechanical properties will be presented in Section IV.

2. Aluminum-1.79 w/o Copper Alloys. Al-1.79 w/o Cu specimens were fractured as solid solution alloys, or containing θ' or θ precipitates employing Instron tensile tests (cross head speed 8 $\mu\text{m}/\text{sec}$) and in-situ HVEM. Macroscopic tests were carried out on flat specimens 1.7 mm thick with a gage length of 40 mm and 12 mm wide; in-situ straining was done on 12 mm x 2 mm x 0.2 mm specimens with a center portion thinned electrolytically. Grain size was 0.1-0.3 mm.

Stress-strain data and fracture surfaces taken by SEM have been published.¹³ It was found that there were more dimples on fracture surfaces of solid solution (ss) treated specimens than on specimens treated for θ' precipitates.

Although the average density of θ' precipitates measured from TEM micrographs was $2.8 \times 10^8 \text{ cm}^{-2}$, the density of the large dimples in the θ' specimens was $2.5 \times 10^5 \text{ cm}^{-2}$, a difference of three orders of magnitude. Furthermore, since the ss specimens were essentially inclusion free within each grain, the formation of this dimple type was evidently unrelated to the presence of θ' precipitates.

The dimples found on the fracture surfaces of the θ specimens were mainly of the equiaxed type. The average dimple density was $5 \times 10^7 \text{ cm}^{-2}$, twice the density of the θ precipitates. Their sizes were much smaller and the dimple density was two orders of magnitude higher than for the ss and θ' specimens.

In-situ fracture observations revealed that all cracks were transgranular and initiated at the thinnest part of the polished area. Microcracks appearing as holes were seen to open up ahead of the advancing crack. The number of holes varied from 3 to 5 with separations ranging from 2 to 4 μm .

The video recordings showed that the crack propagation speeds in the θ' specimens were considerably more uniform than those in the θ specimens. Crack propagation speeds were measured and are listed in Tables III and IV. The cracks in the θ specimens often advanced suddenly over distances of microns. At the end of sudden advances, the crack tip was blunted and thinning ahead of the tip resumed in a slightly different direction. As a consequence the contour of the crack edges were more jagged than for the θ' specimens.

In-situ HVEM experiments also revealed that microcracks were initiated at dark lines which were arranged in cell patterns ahead of the crack tip.²⁶ When examined closer by TEM, these lines were seen as bands and did not represent well-defined sharp boundaries. By tilting the specimen they were confirmed to be due to Bragg diffraction contrast and not to bend contours. Convergent beam micro-diffraction (CBMD) patterns taken from both sides of such a boundary revealed rigid rotations of the same pattern. CBMD patterns from the dark bands exhibited substantially stronger scattering than scattering from areas away from the bands, suggesting the existence of a high dislocation density. The rotation across these boundaries was found to be between 2° and 5° .²⁷

Many fine fringe patterns existed in dark field micrographs of thicker areas. From their relationship with the diffraction vectors

TABLE III

CRACK VELOCITIES IN SPECIMENS CONTAINING θ' PRECIPITATES
DETERMINED FROM VIDEO RECORDINGS OF HVEM IN-SITU EXPERIMENTS

Time Period of Measurement (s)	Magnification of Video Picture ($\times 10^3$)	Crack Velocity (nms^{-1})
50	80	20
45	40	30
200	30	15
15	30	60
80	30	15
90	30	20
90	30	25

TABLE IV

CRACK VELOCITIES IN SPECIMENS CONTAINING θ PRECIPITATES
DETERMINED FROM VIDEO RECORDINGS OF HVEM IN-SITU EXPERIMENTS

Time Period of Measurement (s)	Magnification of Video Picture ($\times 10^3$)	Crack Velocity (nms^{-1})
40	40	50
~0.8	40	7000 ^a
5	20	1500 ^a
75	30	80
40	30	60
0.5	30	13000 ^a
1	30	5000 ^a

^a Velocity measured for sudden crack advances.

these were identified as rotational moiré fringes. Statistics from 86 sets of fringes showed that the majority had spacings between 2 and 4 nm. These corresponded to rotations of $3^\circ - 5^\circ$ between volume elements.²⁷ This is in excellent agreement with the results from SAD and CBMD patterns. However, although the SAD and CBMD patterns revealed misorientations between areas connected two-dimensionally in the image, the moiré fringes originated from misorientations between overlapping areas. The results demonstrated the existence of misoriented volume elements at the crack edge which are three dimensionally connected and separated by high dislocation density boundaries.²⁷ The dislocation density determined from ligament micrographs was in the order of 10^{11} dislocations/cm².

No precipitate was observed to have any specific relationship to hole formation in general. From in-situ observations it is clear that the holes at which fracture was initiated locally must be at some point along the edge of the dragon's teeth. If the hole was caused by interface decohesion, then that initiation site should have been marked by a precipitate. The rarity of such an occurrence in both the θ' and the θ specimens indicated that true interface decohesion rarely occurred.

SECTION IV DISCUSSION

All metals and alloys investigated in this research had typical workhardening characteristics, i.e., they would show stages I, II, and III in their single crystal stress-strain curves with the exception of alloys. This statement puts the focus on basic workhardening phenomena which have been largely neglected in the past in the context of ductile fracture mechanisms. Since rupture, defined as separation at 100% RA, takes place in all ductile fracture, regardless whether at a macroscopic chisel edge or at the separation of ligaments across a void sheet,²⁸ the workhardened state at this point is the most severe a metal or alloy can sustain.

Workhardening must be seen, of course, in the context of the metal's microstructure. Figure 11 should be considered as providing examples of the most important defects which have to be taken into account in the microstructural regime of ductile fracture. In addition, definitions of dislocation arrays should be consulted.²⁹ By choosing pure metals, many complications which develop in order-disorder alloys, two-phase alloys, precipitation and dispersion hardened alloys have been avoided in this research and the discovery of basic phenomena and their role in ductile fracture was facilitated. The early initiation of voids at second phase particles involved in cup-and-cone fracture made it difficult in the past to appreciate workhardening mechanism which lead to dislocation cell walls and point defect clusters. Low energy configurations of dislocation sub-boundaries were explored in depth as early as 1950 by Read and Shockley.^{30,31} Also, extensive X-ray diffraction evidence was available before the TEM of dislocation was

THE MICROSTRUCTURAL REGIME OF DUCTILE FRACTURE

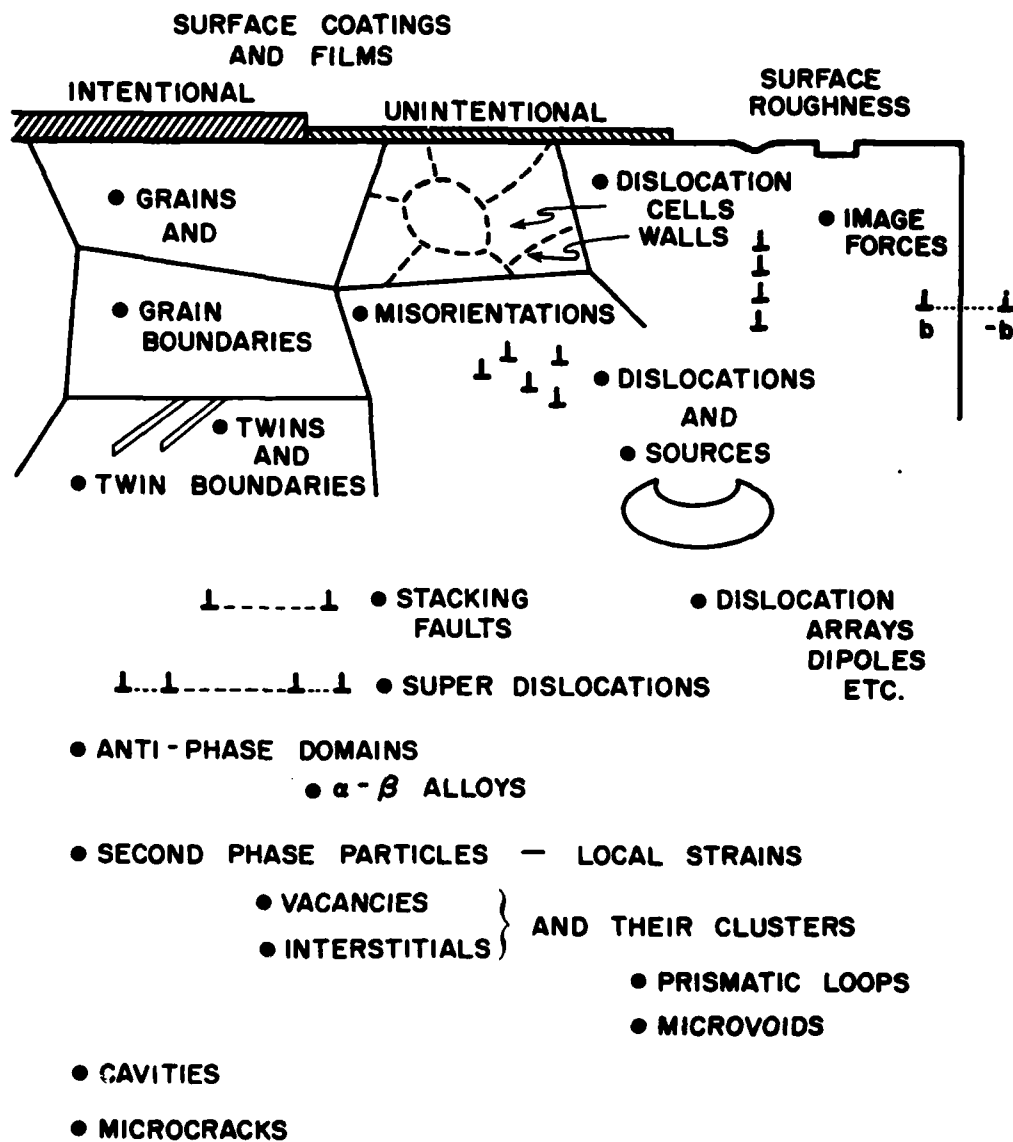


Figure 11. Microstructures Related to Ductile Fracture.

discovered. Cell walls produced by deforming thin foils in an electron microscope were known since 1958,³² and extensive studies of stress field associated with dislocation cell walls were carried out by Kuhlmann-Wilsdorf and coworkers from 1970³³ to 1973;³⁴ a review of substructure strengthening was published by Thompson.³⁵ As discussed by Kuhlmann-Wilsdorf in great detail,³⁶ the reduction of cell diameters levels off in stage III and the workhardening rate is reduced eventually as shown by the parabolic shape of the stress-strain curve. Flow stress σ and cell diameter d are related as

$$\sigma = \sigma_0 + Kd^{-1}$$

with σ_0 the frictional stress and K a constant. Dislocation cell walls also are the boundaries between volume elements that are misoriented against each other. It is important to recall that cell walls have energy associated with them which, at large misorientations, can be considerable.

The role of dislocation cell walls was not immediately obvious from the first experimental results obtained by in-situ HVEM straining to fracture. Videotapes showed thinning in Ag single crystals and 304 stainless steel foils well ahead of the propagating crack. In the electron transparent regions dark lines were visible which changed their positions during the dynamic testing conditions. In Ag crystals it was observed repeatedly that slits suddenly opened up to a length of about 200 nm with a width of about 20 nm. The time interval of the appearance of these microcracks at elongation speeds of 100 nm/sec was in the order of 0.1 seconds. It should be pointed out that this phenomenon of microcrack initiation took place in crystals which were between 1 and 7 μm thick, i.e. a considerable amount of true strain $\epsilon \geq 1$ was involved

before the microcracks appeared. At times, ten or more holes were seen to be in front of the crack tip, their shape broadening in Ag from a slit to a diamond shaped hole as the distance to the crack tip became smaller. The microcracks continued to appear suddenly in the thinned zone about 2 μm to 4 μm ahead of the crack tip. In polycrystalline stainless steel foils of comparable thickness holes of more irregular shape opened up in the semi-transparent areas about 2 μm to 5 μm ahead of the crack tip. As can be seen from Figure 9 the new holes did not appear directly in front of the crack tip but under angles of about 30° . This agrees well with theoretical predictions of the direction and shape of the plastic zone in front of crack tips.³⁷ In electron transparent foils of stainless steel glide dislocations were seen in profusion in a broad plastic zone along the crack about 10 to 15 times the thickness t of the foil in width; with $t = 200\text{ nm}$ up to 500 nm the plastic zone varied between 2 μm and 8 μm . Here, microcracks ahead of the crack tip were produced by continuous thinning as will be discussed in some detail below. If $t < 100\text{ nm}$, as mostly was true near the perforation, cracks were seen to propagate without the involvement of dislocations based on observations that neither the crack flank nor the area ahead of the crack tip contained any dislocations. Cracks were straight within each individual grain and the operating mechanism appears to be comparable to cleavage. It must be concluded that the thickness has a very significant influence on crack initiation processes. This is not unexpected when considering the intimate relationship which must exist between microcrack formation and dislocation behavior. Observations of this kind made it mandatory to investigate only specimens which had a minimum foil thickness that would guarantee dislocation behavior and workhardening, as known from conventional crystal

plasticity. Also, the rate of elongation was found to be of great importance in in-situ fracture experiments and this point will be discussed in a special paragraph.

Careful lattice rotation measurements in the neck of iron whiskers were made by Gardner^{8,16} using the X-ray precession method. X-ray diffraction spots were smoothly and continuously streaked as a result of the rotation of small volume elements. The continuous intensity of the elongated spots is an indication that the resolution of the X-ray technique was insufficient to measure the size of the volume elements although unambiguous data regarding the geometry of glide were obtainable (see Table 5 and Figures 12 and 13). The misorientation between

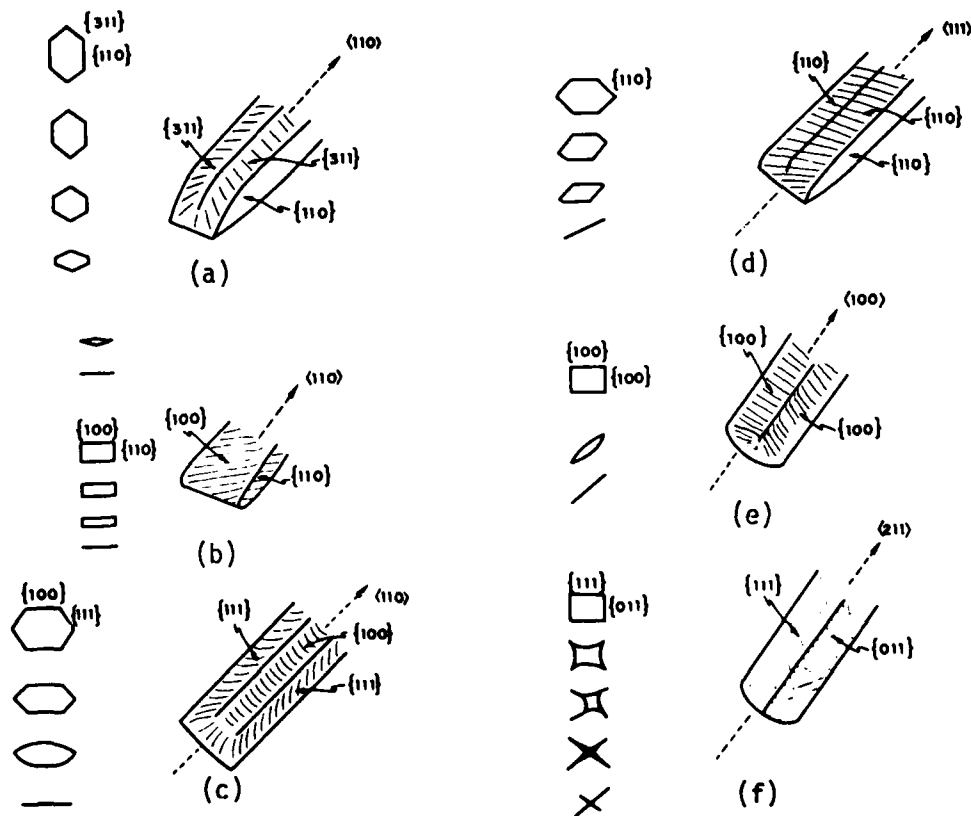


Figure 12. Summary of the Reduction in Area and Cross-Sectional Changes of α -Fe Whiskers. In all cases, the uniform development of a chisel edge is seen.

TABLE V
SUMMARY OF ACTIVE GLIDE SYSTEMS LEADING TO FRACTURE

<u>External Geometry</u>	<u>Tensile Axis</u>	<u>Primary Active Slip System in the Neck of Crystals</u>
A	[011]	$(\bar{2}11)[111]$, $(211)[\bar{1}11]$
glide off*	[011]	$(\bar{1}10)[111]$
B	[011]	$(\bar{1}10)[111]$, $(101)[\bar{1}11]$
C	[011]	$(\bar{1}\bar{1}2)[111]$, $(12\bar{1})[\bar{1}11]$
glide off*	[111]	$(211)[\bar{1}11]$
D	[111]	$(211)[\bar{1}11]$, $(112)[11\bar{1}]$, $(121)[1\bar{1}1]$
glide off*	[001]	$(\bar{1}\bar{2}3)[111]$, $(\bar{1}\bar{1}2)[111]$, $(\bar{2}\bar{1}3)[111]$
E	[001]	$(\bar{1}\bar{1}2)[111]$, $(112)[\bar{1}\bar{1}1]$, $(\bar{1}12)[1\bar{1}1]$, $(1\bar{1}2)[\bar{1}11]$
F	[211]	$(2\bar{1}\bar{1})[111]$, $(112)[11\bar{1}]$, $(121)[1\bar{1}1]$

* If simple glide off were to occur, the active slip system which would be responsible is given.

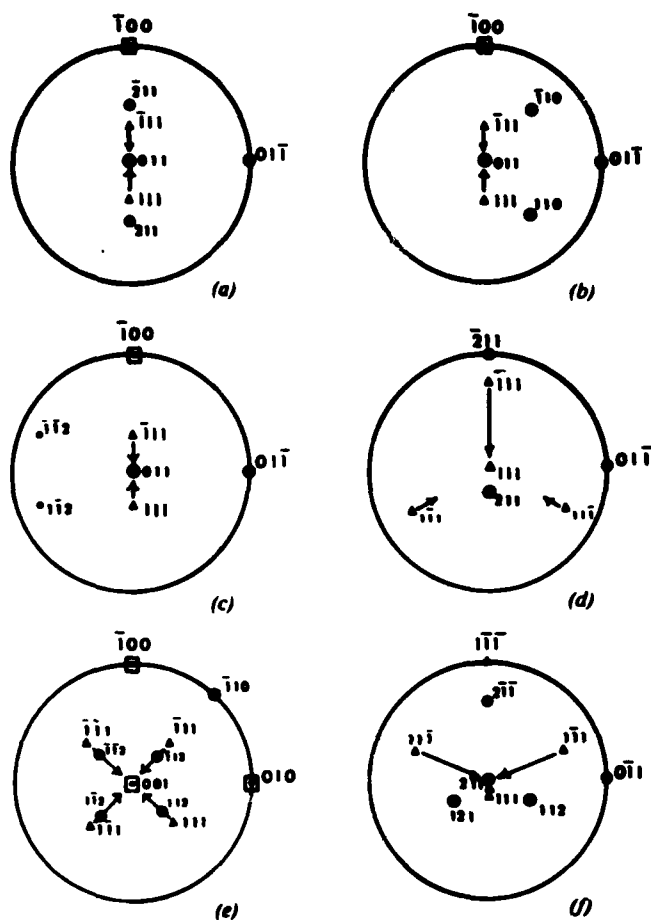


Figure 13. Summary of Burgers Vectors, Active During the Necking Process, that Give Rise to the Experimentally Observed Geometries of Reduction in Areas of Figure 12(a) thru (f). Large lattice rotations invariably are seen to take place about an $\langle 011 \rangle$ axis. One might expect, since these rotations are due to rotating volume elements, that when the degree of rotation is so large as to align the original active slip direction with the tensile axis, the appearance of a polycrystalline texture would result. Hence, it would not be unusual to obtain $\langle 110 \rangle$ texture diffraction patterns from the crack flank of all of these crystals.

volume elements at the crack flank was then measured by HVEM/SAD which confirmed the overall X-ray measurements, which had been found as high as 30° . This data was taken with beam diameters of 500 nm in "thicker" regions which also included evidence for twinning.¹⁷ The large misorientations found at 500 kV were not so frequent at the thinner ligament remnants depending on the sizes and nature of sub-boundaries.¹⁸ A very important conclusion was drawn; namely, that due to the energy available at the boundary between misoriented volume elements a preferred site was created there which could lead to the initiation of a void or a microcrack. If one assumes that the work for fracture W_F equals the newly created surface energy $2\gamma_s$ then

$$W_F = 2\gamma_s - \gamma_b$$

where γ_b is the boundary energy.

Shortly afterwards direct experimental evidence for this contention was obtained by in-situ HVEM fracture studies by Pollock in Be.²¹ Microcracks were seen to open up at dislocation cell walls in the sharp neck. Their lengths were in the order of 0.1 μm but also were observed as long as 1 μm or even exceeding this measure. As seen in Ag before, these microcracks appeared as narrow slits not wider than 50 nm and eventually increased in width. The fact that the initiation of microcracks in specimens 3 to 5 μm thick was detectable, was due to the relatively large cell size which develops when Be crystals are strained parallel to $\{10\bar{1}0\}$ or $\{11\bar{2}0\}$. Sliced parallel to (0001) these crystals deform by prism glide on $\{10\bar{1}0\} \langle 11\bar{2}0 \rangle$.

The cell walls along which microcracks have been seen to originate are lying under angles between 35° and 55° against the stress axis and the microcracks follow the cell walls. A case was observed (Figure 14)

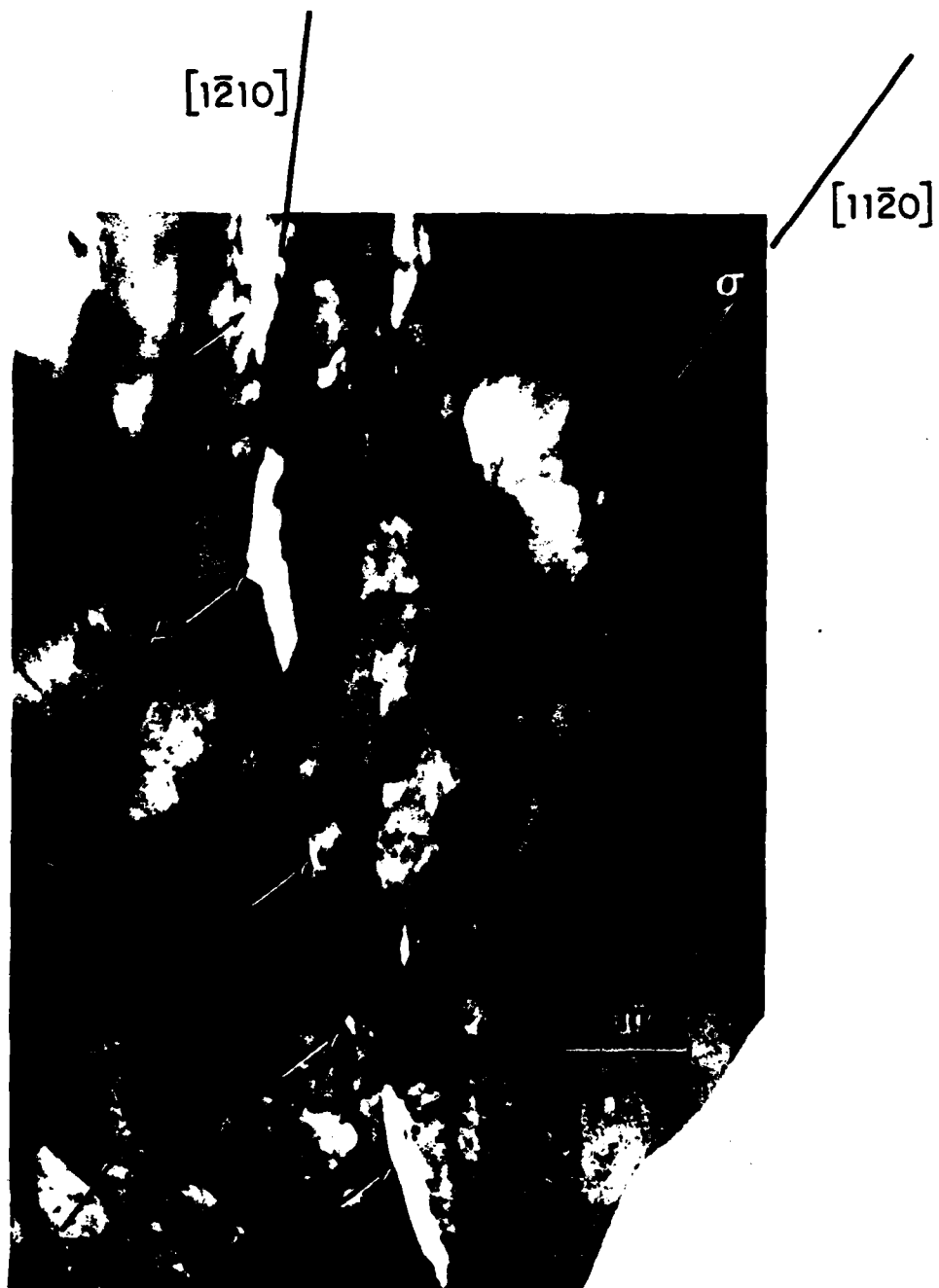


Figure 14. Microcrack Initiation at a Dislocation Cell Wall in $\text{Be}^{(21)}$. Local cleavage is indicated by portion of crack parallel to intersection with $\{11\bar{2}0\}$.

where a larger microcrack had one edge parallel to the line of intersection between (0001) and $\{11\bar{2}0\}$. Since $\{11\bar{2}0\}$ is a type II prism plane, it is a cleavage plane. The probability to have cleavage occurring is fairly high when considering that prism glide at room temperature requires a stress four times higher than basal glide while cleavage on $\{11\bar{2}0\}$ will occur at five times the stress of basal glide.

The misorientation of a tilt boundary is given in first approximation as $\theta \cong b/D$, where b is the Burgers vector and D is the distance between dislocations. In a cell wall the misorientation is not accommodated in one plane but rather over a width, W , containing N excess dislocations

$$\theta \cong \frac{Nb}{ND}.$$

The dislocation density in the boundary is then

$$\rho_b = \frac{N}{ND}$$

Introducing the average distance between dislocations through

$$\rho = \frac{1}{\bar{\ell}^2} \quad \text{we have } \bar{\ell} = \sqrt{WD} \quad \text{and taking } D \text{ from above}$$

$$\bar{\ell} = \frac{\sqrt{Wb}}{\theta}$$

Plotting $\bar{\ell}$ against cell wall width (Figure 15) for boundaries of various misorientations, one sees that in cell walls with $\theta > 10^\circ$ the average link length is below 10 nm for observed wall thicknesses. Since, in accordance with observations in general, the thickness of cell walls decreased with increasing deformation, values of $\bar{\ell} < 5$ nm are highly probable.

For cleavage to take place one must assume that most dislocation sources remain inoperative, i.e. the stress

$$\tau_s = \frac{Gb}{\bar{\ell}} \cong \sigma_c \cong \frac{E}{30},$$

if one assumes for the cleavage stress $\sigma_c \cong E/30$. $\sigma_c = 9.6 \cdot 10^9$ Pa

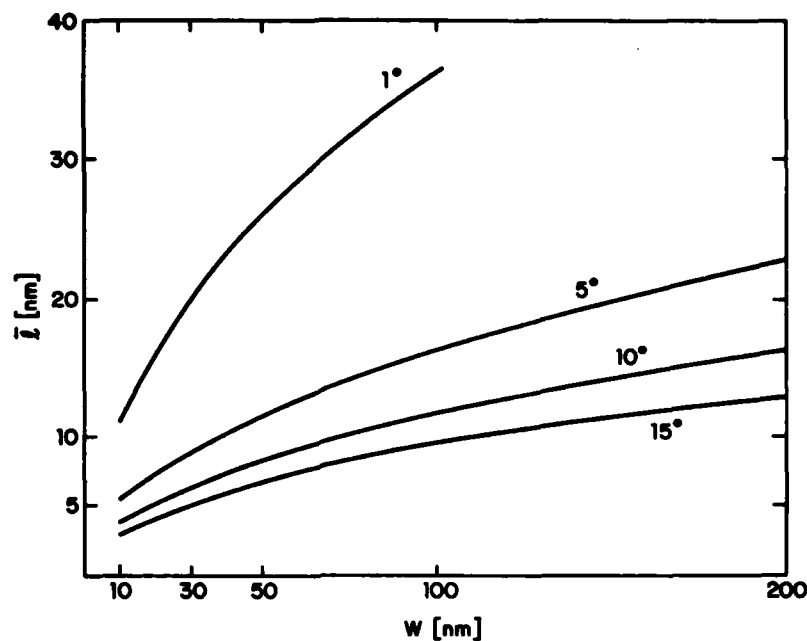


Figure 15. Average Distance between Misorientations \bar{l} in Cell Wall of Width W for Various Misorientations.

while with $\bar{l} = 5$ nm the source stress $\tau_s = 5 \times 10^9$ Pa. The stress concentrations at the ends of the microcrack nucleus will provide the necessary stress increase for reaching σ_c but will not be sufficient to spontaneously create large numbers of dislocations at the tips of the microcrack nucleus. The mechanism for crack initiation given here would fit the observations made on Ag, Be, α = Fe, and 304 stainless steel. The measurements of misorientations between cell walls reported for the pure metals in Section III and the values quoted for Be by Hedke,²⁰ for Al-Cu alloys by Chan²⁶ and for Au⁵ are in support of this view.

Upon further straining microcracks grow by glide processes. A study of hole growth in Ag showed how sensitively this localized process was tied in with the general deformation history of the specimen.¹¹ For example, necking changed the original $\langle 110 \rangle$ stress axis to $\langle 112 \rangle$ on

account of lattice rotations in the necked portion of the crystal where the crack would occur. Further, the development of a series of holes in front of the crack tip created a very complex stress field involving compressive local stresses in addition to the tensile stresses caused by the applied stress. Finally, grip effects on the active glide systems had to be considered.¹⁰ However, this rather complex situation was completely in agreement with crystal plasticity as predicted from known rules, i.e. observation of Schmid's law, motion of tensile axis with increasing deformation, and lowest energy configuration of dislocations in thin specimens. Under these conditions ligaments deformed plastically to elongate and to thin down and eventually to enlarge the microcracks to effect the final coalescence.¹¹

How can these findings, obtained from in-situ electron microscopy be applied to ductile fracture in general? In precipitation or dispersion hardened metals void initiation is caused by second phase particles which may be described as crystal inhomogeneities. Without question, dislocation cell walls can be considered as inhomogeneities in a crystal and, as we have seen, may initiate voids or microcracks.

In pure bulk metals, cell walls are primarily responsible for initiating shallow, almost penny shaped cavities in the sharp neck leading to a number of thin foils in a tensile specimen before the final separation.⁵ This situation may be compared to that which exists in a cup-and-cone fracture when a "void sheet" has developed; here, thin ligaments hold the sample before rupture of these ligaments. Based on various measurements, the ligaments will thin down by plastic deformation to about 100 nm and the final process for separation will begin.

At this stage the deformation will take place at the condition of plane stress and dislocation motion will produce through-thickness glide. This also satisfies the low energy requirement for dislocations in thin foils. Depending on the mechanism to provide glide dislocations, two glide systems will be activated in most cases. Specifics have been worked out for the final separation in Au.⁵ Here, the thin foils in the sharp neck are oriented parallel to (110) and the stress axis will be close to $[\bar{3}35]$ or $[\bar{2}23]$. Under these conditions (111)[10 $\bar{1}$] and ($\bar{1}\bar{1}$ 1)[011] have the highest shear stress and will be activated. Thinning parallel to $[\bar{1}10]$ takes place, resulting in a microcrack parallel to this direction which is borne out by the triangular shape of the ligament remnant. The other direction is $[\bar{1}12]$ which follows from the intersection of (110) and ($\bar{1}\bar{1}$ 1), a plane which is perpendicular to (110) as seen in Figure 4. Glide on (111) and ($\bar{1}\bar{1}$ 1) and the development of a microcrack parallel to $[\bar{1}10]$ resulted in a local stress direction change so that the axis between microcracks will now be near $[\bar{3}32]$ or $[\bar{2}21]$, and the glide systems ($\bar{1}\bar{1}$ 1)[$\bar{1}01$], $[0\bar{1}\bar{1}]$ and the twinning system ($\bar{1}\bar{1}$ 1)[$\bar{1}12]$ have then the highest resolved shear stress. And indeed shear by translation and twinning on these systems has been observed.⁵ The last step produced the final separation in the form of a zig-zag crack.

The last paragraphs discussed two mechanisms for crack initiation: (1) microcrack formation at dislocation cell walls; (2) microcrack formation due to thinning. In the latter case the dislocation activities occurred in thin foils governed by rules that could deviate from the motion and interaction of dislocations in bulk materials. For example, in thin specimens the clustering of point defects will be different and also, in general, cell walls will be absent. However, one has to distinguish the plastic deformation in thin foils of undeformed metal from that

in materials which suffered a substantial amount of true strain, say $\epsilon > 1, 2$, or more. In these, dislocations, point defects, vacancy clusters and cell wall remnants can be expected to still be present. In Au it was found that a high density of stacking fault tetrahedra was contained in electron transparent parts of the crack flank as well as voids of 5 nm to 10 nm in diameter. It was noted that the availability of small voids and degenerated dislocation arrays from cell walls formed in thicker material, acted as modifiers of the geometry of the crack flank⁵ in that they prevented the sharp triangular ligaments from being formed. The thin foils or ligaments holding the specimen together in the sharp neck are mostly of uniform thickness, although numerous shallow dimples can be seen by TEM. These areas must have been produced by glide and therefore their surfaces are characterized by steps where dislocations had left the crystal. Vicinal surfaces are likely locations for spontaneous dislocation formation,³⁸ in particular if the material increases in thickness in a low angle wedge-like fashion. From all TEM observations this seems to be the case and it was proposed that the vicinal surface of shallow dimples is the location for spontaneous dislocation production. It was estimated that approximately 700 glide dislocations would be needed to thin down a ligament which would result in a microcrack parallel to $[\bar{1}10]$.⁵

The discovery of small voids in ligament remnants of Au gives credence to a proposal made on the basis of measurements obtained from fracture surfaces of stainless steel, namely that small voids due to the clustering of vacancies are participating in crack nucleation.²⁵ The large number of stacking fault tetrahedra at the crack flanks of Au and Cu and the presence of voids in Al are in support of this contention.

The energy of a dislocation cell wall in comparison with the interfacial energy of θ' precipitates in an Al-1.8 w/o Cu alloy was considered by Chan.^{13,26} If one describes microcrack or void initiation by an empirical probability function $\exp(-CU)$ with C a constant and U the total energy of decohesion, one would have to subtract from U any energy U^* that would be available in the form of interfacial energy or the energy of dislocation cell walls. An estimate of the interfacial energy of θ' precipitates based on literature data^{39,40} yields about 0.3 Jm^{-2} .

The misorientation between adjacent dislocation cells in these alloys was usually between 2° and 5° . If the boundaries of the cells were of the simple tilt or twist type, this corresponds to an energy of approximately $0.2 - 0.26 \text{ Jm}^{-2}$. However, there are three important facts that must be taken into consideration.

- (1) Numerical values of the misorientations are based on projections; therefore this represents lower limits.
- (2) The boundaries actually consisted of high density dislocation tangles and therefore their energies will be higher than that of a simple tilt or twist boundary with the same misorientation.
- (3) The boundaries analyzed in the post-fracture studies were those that were left behind after fracture, while those that had initiated the microcracks had mainly dissociated. Evidently, the original boundaries must have possessed higher energies and higher dislocation densities, rendering them energetically favorable decohesion sites.

The dislocation density at the microcrack initiation site can be estimated through the flow-fracture $(\tau - \sigma_f)$ stress expression.

$$\tau = \alpha G b \rho^{\frac{1}{2}}$$

where G is the shear modulus and α is approximately 0.4. By setting τ equal to $\sigma_f = 470 \text{ MPa}$, ρ was computed to be $2.4 \times 10^{12} \text{ cm}^{-2}$. The stored energy given by the expression³⁶

$$U_{st} = \rho \frac{Gb^2}{4} \ln \left(\frac{\rho^{\frac{1}{2}}}{b} \right)$$

yields $U_{st} = 1.3 \times 10^5 \text{ Jm}^{-3}$.

From in-situ experiments the boundaries where microcracks had been initiated were approximately 0.1 μm wide. Thus the two-dimensional projected energy density at the microcrack initiation site will be 1.3 Jm^{-2} . For θ precipitates the corresponding values are $\sigma_f = 220 \text{ MPa}$, $\rho = 5.4 \times 10^{11} \text{ cm}^{-2}$ and $U_{st} = 3.5 \times 10^4 \text{ Jm}^{-3}$, and the projected energy density is 0.35 Jm^{-2} .

Although these numbers are only empirical estimates, they seemed to be representative for the reason that the calculated dislocation density agreed well with dislocation density data. Also, the results of this investigation that microcrack initiation sites were located primarily at dislocation boundaries agreed with the relative magnitudes of available energy densities estimated for dislocation boundaries and precipitate-matrix interfaces.

It is tempting to think of crack propagation and of the growth of voids of microcracks in terms of single dislocations being emitted at the crack tip or moving into the crack flank. There is one problem with that approach in that the crosshead speed, in order to record individual dislocations, has to be as low as 10 nm/sec or even lower. While such a low strain rate does not pose a problem with the in-situ straining devices, it must be realized that crosshead speeds in testing machines are around 10 $\mu\text{m}/\text{sec}$. The difference in strain rates then amounts to three orders of magnitude and it was found that indeed a crosshead speed of 10 nm/sec changed the mode of crack propagation noticeably when compared to higher speeds as first observed on single crystals of Ag in 1972.⁴¹ Almost all metals and alloys investigated

under this contract were subjected during in-situ straining to crosshead speeds of 0.01 $\mu\text{m}/\text{sec}$ within the framework of the experiments, and the motion of single dislocations near the crack tip was seen and recorded.

However, since it was the objective of this research to develop mechanisms of ductile fracture in general, i.e., in bulk materials and not just in thin foils, most of the work was carried out at crosshead speeds of about 1-10 $\mu\text{m}/\text{sec}$. The results recorded and discussed in this report were all obtained at strain rates comparable to those in conventional Instron tests. Then one finds that most crack flanks are exhibiting zig-zag features many of whom have edges parallel to low indexed crystallographic directions. At very low crosshead speeds, holes rarely open up in front of the crack tip and the crystallographic nature of the crack flank was lost; occasionally, the separation of the metal was observed to be by shear. If holes are opening up in front of the tip at very low rates, they are roundish and the electron transparent area in Au, for example, shows an appreciable number of dislocation cell walls which at higher speeds are absent.¹² It must be clear by now that there is locally a continuous interplay between crack propagation motion and microcrack blunting which affects the rate of propagation from point to point. An example is provided by Chan^{13,26} in Tables III and IV. Here one sees the change of crack velocities within each of two alloys of Al-1.8 w/o Cu heat treated for θ' and θ precipitation. The effect of different types of precipitates is quite noticeable. The crack propagation mechanism as affected by crack velocity deserves more attention in future research. It is specifically mentioned in this report to alert the reader that the observations near crack tips in in-situ experiments are strongly influenced by crosshead speeds, in

particular in the range from 1 $\mu\text{m}/\text{sec}$ to 0.01 $\mu\text{m}/\text{sec}$ which normally results in very slow crack tip movements, depending on the specific metal or alloy and their thermal history.

SECTION V

CONCLUSIONS

1. The deformation history of pure metals and alloys plays a major role in all phases of ductile fracture. The specific workhardening characteristics affect microcrack initiation and crack propagation in the FCC, BCC, and HCP systems investigated.
2. The development of a dislocation cell structure during workhardening has a profound influence on crack initiation and propagation.
3. Misorientations between cells of up to 30° are accommodated by cell boundaries which have high energies. Microcrack initiation takes place at these cell boundaries.
4. Experimental evidence has been provided that microvoids and cleavage are participating in the mechanism of crack initiation at cell walls.
5. It is concluded that in bulk specimens microcracks are initiated at cell walls which then grow into penny-shaped cracks in the sharp neck before rupture. At that point in the fracture process, ligaments approximately 0.1 μm thick hold the specimen together.
6. Ligaments are ruptured by shear which in low stacking fault materials can involve twinning, resulting in a zig-zag fracture flank.
7. Lattice defects, microvoids and cell wall remnants can affect the rupture process in thin ligaments which, in general, proceeds in accordance with the known rules of crystal plasticity.
8. In alloys containing soft second phase particles void initiation takes place predominantly at dislocation cell walls. The primary role of the particles is their involvement in the formation of cell walls.
9. Regardless whether fracture occurs macroscopically in the rupture mode or by cup-and-cone fracture, the final separation is by rupture, since the void sheet consists of a multitude of thin ligaments.
10. In-situ HVEM studies have been instrumental in the discovery that dislocation cell walls are the most important sites for microcrack initiation and are affecting crack propagation in a substantial manner. The study of ductile fracture in the microstructural regime also requires determinations of mechanical properties, SEM, analytical TEM and X-ray microanalysis.

ACKNOWLEDGEMENT

It is a pleasure to acknowledge the contributions made by Dr. P. Clarkin, Materials Division, Office of Naval Research, Arlington, Virginia, to this research project. I am grateful for his continued interest and many valuable scientific discussions regarding this research throughout the years.

REFERENCES

1. H. C. Rogers, Transactions of the AIME, Vol. 218 (1960), p. 498.
2. K. E. Puttick, Phil. Mag., Vol. 4 (1959), p. 964.
3. C. Crussard, R. Borione, J. Plateau, Y. Morillon, and F. Maratray, Journal of Iron and Steel Institute, Vol. 183 (London, 1956), p. 146.
4. G. LeRoy, J. D. Embury, G. Edwards, and M. F. Ashby, Acta Met., Vol. 29 (1981), p. 1509.
5. H. G. F. Wilsdorf, Acta Met., Vol. 30 (1982), in press.
6. H. G. F. Wilsdorf, Rev. Sci. Instr., Vol. 29 (1958), p. 323.
7. R. W. Bauer, R. L. Lyles and H. G. F. Wilsdorf, Zs. Metallkd., Vol. 63 (1972), p. 525.
8. R. N. Gardner and R. H. Hanscom, Materials Science Engineering, Vol. 22 (1976), p. 167.
9. R. N. Gardner and H. G. F. Wilsdorf, Fracture 1977, D. M. R. Taplin, ed., U. Waterloo Press, 1977, Canada, p. 349.
10. R. L. Lyles, Jr., M.S. Thesis, University of Virginia, 1971.
11. R. L. Lyles, Jr. and H. G. F. Wilsdorf, Acta Met., Vol. 23 (1975), p. 269.
12. H. G. F. Wilsdorf, to be published.
13. I. Y. T. Chan and H. G. F. Wilsdorf, Materials Science Engineering, Vol. 49 (1981), p. 229.
14. R. N. Gardner, Journal of Crystal Growth, Vol. 43 (1978), p. 425.
15. R. N. Gardner and H. G. F. Wilsdorf, Met. Trans., Vol. A11 (1980), p. 653.
16. R. N. Gardner, M.S. Thesis, University of Virginia, 1975.
17. R. N. Gardner, Ph.D. Dissertation, University of Virginia, 1977.
18. R. N. Gardner and H. G. F. Wilsdorf, Met. Trans., Vol. A11 (1980), p. 659.
19. T. C. Pollock, M.S. Thesis, University of Virginia, 1974.

20. D. E. Hedke, M.S. Thesis, University of Virginia, 1979.
21. T. C. Pollock, Ph.D. Dissertation, University of Virginia, 1977.
22. R. N. Gardner, T. C. Pollock, and H. G. F. Wilsdorf, Materials Science Engineering, Vol. 29 (1977), p. 169.
23. R. W. Bauer, Ph.D. Dissertation, University of Virginia.
24. R. W. Bauer and H. G. F. Wilsdorf, Dynamic Crack Propagation, G. C. Sih, ed., Noordhoff Int. Publ., 1973, Leyden, p. 197.
25. R. W. Bauer and H. G. F. Wilsdorf, Scripta Met., Vol. 7 (1973), p. 1213.
26. I. Y. T. Chan, Ph.D. Dissertation, University of Virginia (1980).
27. I. Y. T. Chan and H. G. F. Wilsdorf, Acta Met., Vol. 29 (1981), p. 1221.
28. H. G. F. Wilsdorf, Krist. und Techn., Vol. 14 (1979), p. 1265.
29. J. T. Fourie, P. J. Jackson, D. Kuhlmann-Wilsdorf, D. A. Rigney, J. H. van der Merwe, and H. G. F. Wilsdorf, Scripta Met., Vol. 16 (1982), p. 157.
30. W. T. Read and W. Shockley, Phys. Rev., Vol. 78 (1950), p. 275.
31. W. T. Read and W. Shockley, Imperfections in Nearly Perfect Crystals, W. Shockley, ed., Chapter 13, Wiley, 1952, New York.
32. H. G. F. Wilsdorf, ASTM Spec. Techn. Publ., Vol. 245 (1958), p. 43.
33. J. T. Moore and D. Kuhlmann-Wilsdorf, J. Appl. Phys., Vol. 41 (1970), p. 4411.
34. M. N. Bassim and D. Kuhlmann-Wilsdorf, Phys. Stat. Sol. A, Vol. 19 (1973), p. 335; for other references see 35.
35. A. W. Thompson, Met. Trans., Vol. A8 (1977), p. 833.
36. D. Kuhlmann-Wilsdorf, Workhardening, J. P. Hirth and J. Weertman, eds., Gordon and Breach, New York, 1968, p. 97.
37. G. T. Hahn and A. S. Rosenfield, ASTM Spec. Techn. Publ., Vol. 432 (1968), p. 5.
38. J. P. Hirth, Relation Between Structure and Strength in Metals and Alloys, H.M.S.O., London, 1963, p. 218.
39. J. D. Boyd and R. B. Nicholson, Acta Met., Vol. 19 (1971), p. 1101.

40. H. B. Aaron and H. I. Aaronson, Acta Met., Vol. 18 (1970), p. 699.
41. R. L. Lyles and H. G. F. Wilsdorf, Proc. 30th Annual EMSA Meeting (1972), p. 670.

APPENDIX I

List of Metals and Alloys Studied in Chronological Order

1970-1971	Ag, Whiskers
1972-1975	304 Stainless Steel (extra pure stock), Polycryst.
1974-1977	Be, single crystals
1975-1977	α -Fe, Whiskers
1978-1982	Al-1.8 w/o Cu (sol. sol., G. P. Zones, θ' , θ)
1980-1981	Al (high purity)
1980-1982	Au (99.9999)
1981	Cu (99.999)

DISTRIBUTION LIST

Copy No.

1 - 6	Office of Naval Research Department of the Navy 800 North Quincy Street Arlington, VA 22217 Attention: Metallurgy Division Code 471
7 - 8	Mr. C. Richard Main ONR Resident Representative 2110 G Street, N.W. Washington, D.C. 20037
9 - 10	H. G. F. Wilsdorf
11	K. R. Lawless
12 - 13	E. H. Pancake Sci/Tech Information Center
14 - 92	ONR Distribution (Addresses Attached)
93	RLES Files

D#262R
2248:LLL

Defense Documentation Center
Cameron Station
Alexandria, VA 22314

Naval Air Propulsion Test Center
Trenton, NJ 08628
Attention: Library

Office of Naval Research
Department of the Navy
800 N. Quincy Street
Arlington, VA 22217
Attention: Code 471

Naval Construction Battalion
Civil Engineering Laboratory
Port Hueneme, CA 93043
Attention: Materials Division

Office of Naval Research
Department of the Navy
800 N. Quincy Street
Arlington, VA 22217
Attention: Code 102

Naval Electronics Laboratory
San Diego, CA 92152.
Attention: Electron Materials
Sciences Division

Office of Naval Research
Department of the Navy
800 N. Quincy Street
Arlington, VA 22217
Attention: Code 470

Naval Missile Center
Materials Consultant
Code 3312-1
Point Mugu, CA 92041

Commanding Officer
Office of Naval Research
Branch Office
Building 114, Section D
666 Summer Street
Boston, MA 02210

Commanding Officer
Naval Surface Weapons Center
White Oak Laboratory
Silver Spring, MD 20910
Attention: Library

Commanding Officer
Office of Naval Research
Branch Office
536 South Clark Street
Chicago, IL 60605

David W. Taylor Naval Ship
Research and Development Center
Materials Department
Annapolis, MD 21402

Naval Undersea Center
San Diego, CA 92132
Attention: Library

Naval Research Laboratory
Washington, DC 20375
Attention: Code 6000

Naval Underwater System Center
Newport, RI 02840
Attention: Library

Naval Research Laboratory
Washington, DC 20375
Attention: Code 6100

Naval Weapons Center
China Lake, CA 93555
Attention: Library

Naval Research Laboratory
Washington, DC 20375
Attention: Code 6300

Naval Postgraduate School
Monterey, CA 93940
Attention: Mechanical Engineering
Department

Naval Research Laboratory
Washington, DC 20375
Attention: Code 6400

Naval Research Laboratory
Washington, DC 20375
Attention: Code 2627

Naval Air Development Center
Code 302
Warminster, PA 18964
Attention: Mr. F. S. Williams

NASA Headquarters
Washington, DC 20546
Attention: Code RRM

Naval Air Systems Command
Washington, DC 20360
Attention: Code 52031

Naval Air Systems Command
Washington, DC 20360
Attention: Code 52032

Naval Sea System Command
Washington, DC 20362
Attention: Code 035

NASA Lewis Research Center
21000 Brookpark Road
Cleveland, OH 44135
Attention: Library

Naval Facilities Engineering
Command
Alexandria, VA 22331
Attention: Code 03

National Bureau of Standards
Washington, DC 20234
Attention: Metallurgy Division

Scientific Advisor
Commandant of the Marine Corps
Washington, DC 20380
Attention: Code AX

Director Applied Physics Laboratory
University of Washington
1013 Northeast Fortieth Street
Seattle, WA 98105

Naval Ship Engineering Center
Department of the Navy
Washington, DC 20360
Attention: Code 6101

Defense Metals and Ceramics
Information Center
Battelle Memorial Institute
505 King Avenue
Columbus, OH 43201

Army Research Office
P.O. Box 12211
Triangle Park, NC 27709
Attention: Metallurgy & Ceramics Program

Metals and Ceramics Division
Oak Ridge National Laboratory
P.O. Box X
Oak Ridge, TN 37380

Army Materials and Mechanics
Research Center
Watertown, MA 02172
Attention: Research Programs Office

Los Alamos Scientific Laboratory
P.O. Box 1663
Los Alamos, NM 87544
Attention: Report Librarian

Air Force Office of Scientific
Research
Building 410
Bolling Air Force Base
Washington, DC 20332
Attention: Chemical Science Directorate

Argonne National Laboratory
Metallurgy Division
P.O. Box 229
Lemont, IL 60439

Air Force Materials Laboratory
Wright-Patterson Air Force Base
Dayton, OH 45433

Brookhaven National Laboratory
Technical Information Division
Upton, Long Island, NY 11973
Attention: Research Library

Library
Building 50, Room 134
Lawrence Radiation Laboratory
Berkeley, CA

Office of Naval Research
Branch Office
1030 East Green Street
Pasadena, CA 91106

Dr. T. R. Beck
Electrochemical Technology Corporation
10035 31st Avenue, NE
Seattle, Washington 98125

Professor R. H. Heidersbach
University of Rhode Island
Department of Ocean Engineering
Kingston, Rhode Island 02881

Professor I. M. Bernstein
Carnegie-Mellon University
Schenley Park
Pittsburgh, Pennsylvania 15213

Professor H. Herman
State University of New York
Material Sciences Division
Stony Brook, New York 11794

Professor H. K. Birnbaum
University of Illinois
Department of Metallurgy
Urbana, Illinois 61801

Professor J. P. Hirth
Ohio State University
Metallurgical Engineering
Columbus, Ohio 43210

Dr. Otto Buck
Rockwell International
1049 Camino Dos Rios
P.O. Box 1085
Thousand Oaks, California 91360

Dr. D. W. Hoeppe
University of Missouri
College of Engineering
Columbia, Missouri 65201

Dr. David L. Davidson
Southwest Research Institute
8500 Culebra Road
P.O. Drawer 28510
San Antonio, Texas 78284

Dr. E. W. Johnson
Westinghouse Electric Corporation
Research and Development Center
1310 Beulah Road
Pittsburgh, Pennsylvania 15235

Dr. D. J. Duquette
Department of Metallurgical Engineering
Rensselaer Polytechnic Institute
Troy, New York 12181

Professor R. M. Latanision
Massachusetts Institute of Technology
77 Massachusetts Avenue
Room E19-702
Cambridge, Massachusetts 02139

Professor R. T. Foley
The American University
Department of Chemistry
Washington, D.C. 20016

Dr. F. Mansfeld
Rockwell International Science
Center
1049 Camino Dos Rios
P.O. Box 1085
Thousand Oaks, California 91360

Mr. G. A. Gehring
Ocean City Research Corporation
Tennessee Avenue & Beach Thorofare
Ocean City, New Jersey 08226

Professor A. E. Miller
University of Notre Dame
College of Engineering
Notre Dame, Indiana 46556

Dr. J. A. S. Green
Martin Marietta Corporation
1450 South Rolling Road
Baltimore, Maryland 21227

Dr. Jeff Perkins
Naval Postgraduate School
Monterey, California 93940

Professor H. W. Pickering
Pennsylvania State University
Department of Material Sciences
University Park, Pennsylvania 16802

Professor R. W. Staehle
Ohio State University
Department of Metallurgical
Engineering
Columbus, Ohio 43210

Dr. E. A. Starke, Jr.
Georgia Institute of Technology
School of Chemical Engineering
Atlanta, Georgia 30332

Dr. R. P. Wei
Lehigh University
Institute for Fracture and
Solid Mechanics
Bethlehem, Pennsylvania 18015

Dr. William R. Prindle
National Academy of Sciences
National Research Council
2101 Constitution Avenue
Washington, DC 20418

National Bureau of Standards
Washington, DC 20234
Attention: Inorganic Materials Division

Air Force Office of Scientific
Research
Building 410
Bolling Air Force Base
Washington, DC 20332
Attention: Electronics & Solid State
Sciences Directorate

UNIVERSITY OF VIRGINIA
School of Engineering and Applied Science

The University of Virginia's School of Engineering and Applied Science has an undergraduate enrollment of approximately 1,450 students with a graduate enrollment of approximately 500. There are 125 faculty members, a majority of whom conduct research in addition to teaching.

Research is an integral part of the educational program and interests parallel academic specialties. These range from the classical engineering departments of Chemical, Civil, Electrical, and Mechanical and Aerospace to departments of Biomedical Engineering, Engineering Science and Systems, Materials Science, Nuclear Engineering and Engineering Physics, and Applied Mathematics and Computer Science. In addition to these departments, there are interdepartmental groups in the areas of Automatic Controls and Applied Mechanics. All departments offer the doctorate; the Biomedical and Materials Science Departments grant only graduate degrees.

The School of Engineering and Applied Science is an integral part of the University (approximately 1,500 full-time faculty with a total enrollment of about 16,000 full-time students), which also has professional schools of Architecture, Law, Medicine, Commerce, Business Administration, and Education. In addition, the College of Arts and Sciences houses departments of Mathematics, Physics, Chemistry and others relevant to the engineering research program. This University community provides opportunities for interdisciplinary work in pursuit of the basic goals of education, research, and public service.

DATE
FILME
—8